Micro/Meso Scales Characterization of Alkali-Activated Fly Ash-Slag Concrete Under Sustained High-Temperatures with X-CT, MIP, and SEM Tests

Hongqiang Ma[1,4], Congcong Fu[1], Jialong Wu[1], Xinhua Yuan[1], Chao Wu[2*], Jingjing Feng[3*]

1 College of Civil Engineering and Architecture, Hebei University, Baoding, 071002, China

2 Department of Civil and Environmental Engineering, Imperial College London, South Kensington Campus, London SW7 2AZ, UK

3 College of Water Conservancy and Civil Engineering, Shandong Agricultural University, Taian, Shandong, 271018, China

4 Technology Innovation Center for Testing and Evaluation in Civil Engineering of Hebei Province, Hebei University, Baoding, 071002, China

Corresponding author: *c.wu@imperial.ac.uk; fengjingjing@sdau.edu.cn*

Abstract: Based on X-CT, MIP, and SEM tests, the micro/meso scales evolutions of alkali-activated fly ash-slag (AAFS) concrete under sustained high temperatures are studied. The results show that the water loss of the C-S-H and C-A-S-H gel phases at 60°C is continuous (about 60d). The variation law of meso-scale pore volume based on the X-CT test is consistent with that of micro-scale pore volume obtained by the MIP test. The 2D fractal dimension can be used to qualitatively evaluate the internal micro-cracks and microstructure complexity of AAFS concrete after sustained high-temperature action. The mass loss rate can reach stability within 3d-7d under the action of 100°C, 150°C, and 200°C, and there is no cumulative effect of micro-cracks and pores caused by initial water loss. Under sustained high-temperatures, the internal pore structure, micro-cracks, and microstructure changes of AAFS concrete are persistent, and these persistent changes lead to a significant change in the mechanical properties of AAFS concrete.

Keywords: sustained high-temperatures; alkali-activated fly ash-slag; meso scale; fractal dimension; pore structure

1. Introduction

Cement production is a recognized source of carbon emissions from building materials, accounting for about 8% of the total carbon emissions [1,2]. With the global consensus on carbon reduction, carbon reduction, researchers are trying to find building materials and preparation processes to reduce carbon footprint [3,4]. Alkali-activated materials are a mixture of solid waste with potential pozzolanic activity and alkaline activators [5], which can completely replace cement and have become the most promising cement substitutes, and have produced a lot of positive results in the academic community [6-8]. Compared with cement, alkali-activated cementitious materials can reduce CO_2 emissions by 60%~80% [9,10], and the production cost can be reduced by 7.6%~27% [11]. Alkali-activated materials have obvious advantages such as early strength, chemical attack resistance, and high-temperature resistance [12,13]. However, due to the lack of research on the structural engineering level, the technical standards and specifications of alkali-activated concrete are hindered, resulting in great difficulties in the promotion and application of alkali-activated materials in structural engineering.

The high-temperature effect is one of the working conditions of concrete. At present, the high-temperature effect of alkali-activated materials/concrete is mostly focused on short-term high-temperature action, simulating fire or explosion environment, and the maximum temperature can reach 800°C~1200°C, and the action time is generally 1h~3h [14-16]. However, the operating temperature of many high-temperature workshops, high geothermal tunnels, high-temperature well cementing cement pastes, and concrete spent fuel storage tanks is generally up to 60°C~200°C. The high-temperature duration in such working conditions is very long, which may lead to the concrete entire life cycle remaining in a sustained high-temperature environment. The research group has conducted a preliminary study on the hydration products and pore structure characteristics of alkali-activated cementitious materials under 60°C~250°C [17]. The entire study lasted for 28d at high temperatures, and the duration is relatively short, without considering the heterogeneity of concrete. In addition, there are few related academic achievements. Slag and fly ash are common precursor materials, and there is the most research on alkali-activated fly ash, slag, and fly ash-slag systems [18-20]. C-(A)-S-H gel and N-A-S-H gel are the main hydration products of the alkali-activated fly ash-slag (AAFS) system, and the water loss and morphological changes of hydration products under high temperatures directly affect the macroscopic properties. The free water loss of C-(A)-S-H gel occurs at 60°C~100°C. With the increase of temperature (100°C~300°C), the interlayer water and bound water gradually lose, transform into anhydrous calcium silicate, and part of the gel phase decomposes [21]. The structure of N-A-S-H gel is relatively stable at high temperatures and generally does not decompose [22]. However, under sustained high temperatures, the interaction between various components inside concrete becomes more intense and lasting, and short-term high-temperature effects are difficult to reflect this accumulation effect.

Due to the violent crushing, high-pressure mercury intrusion, and the "ink bottle" effect, the pore data tested by mercury intrusion porosimetry (MIP) deviated from the actual pore structure [23,24]. X-ray computed tomography (X-CT) is a three-dimensional non-destructive imaging technique for observing the interior of an object. A series of X-ray images are obtained through slice scanning, and the images are reconstructed based on threshold and binarization processes. Due to the gray value of each concrete component changing greatly, the pore characteristics, micro-cracks, and interfacial transition zone (ITZ) can be quantified by digital image processing to segment pores, mortar, and aggregates. The microscopic volume obtained by the MIP test can be used to represent the pores [25]. Dong et al. [26] found that the pores (>10μm) detected by MIP test and X-CT are equivalent. Xue et al. [27] found that the voxel size of X-CT affects the details of the microstructure. When the voxel size is 1.5μm^3, the fractal dimensions of micro-scale pores and cracks measured by MIP data are close to those based on X-CT images. X-CT technology can effectively evaluate the meso-scale pore structure characteristics and crack evolution process of concrete [28,29].

This study focuses on AAFS concrete, with fly ash-slag mass ratios (1:0, 1:3, 1:1, 3:1, and 0:1), activator modulus (0.5, 1.0, 1.5, and 2.0), and Na_2O concentration (4%, 6%, and 8%) as research variables. Temperature levels are set at 60℃, 100℃, 150℃, and 200℃, and the duration of high temperature is set at 0d, 3d, 7d, 28d, 60d, and 90d. The compressive strength and mass loss rate of concrete are tested, and the micro/meso scales evolution mechanisms of AAFS concrete are characterized based on X-CT, MIP, and scanning electron microscope (SEM).

2. Materials and methods

2.1. Raw materials

The raw materials used in the test are Class F fly ash and S95 slag, and the chemical compositions of the raw materials obtained by X-ray fluorescence spectroscopy are shown in Table 1. The particle size distribution curves of fly ash and slag are shown in Fig.1, and the median particle size d50 is 19.064μm and 10.529μm, respectively. XRD patterns of fly ash and slag tested by X-ray diffractometer (XRD) are shown in Fig.2. The main components of fly ash are SiO_2 and Al_2O_3, and the mineral components of slag are melilite containing silicon, aluminum, calcium, and magnesium elements. The microscopic morphology of the two raw materials is tested by SEM, as shown in

Fig.3. It can be seen that most of the fly ash is in the form of microspheres with different particles, and the slag is amorphous and does not contain regular crystals. Standard river sand with a fineness modulus of 2.70 is selected as fine aggregate, and ordinary gravel with a continuous gradation of 5mm and 12mm is selected as coarse aggregate. Solid sodium hydroxide (NH, ≥96%) and liquid sodium water glass (NS, 8.5% Na_2O, 26.5% SiO_2 and 65% H_2O) are used as alkali activators. Isopropanol chemical pure is used for the termination hydration of the sample.

Table 1. Chemical compositions of the raw materials (wt%) [30]

Materials	CaO	MgO	Al_2O_3	SiO_2	Fe_2O_3	SO_3	LOI
Fly ash	0.85	5.17	32.7	56.11	3.01	0.65	1.51
Slag	35.58	7.16	16.32	36.10	0.23	1.71	2.9

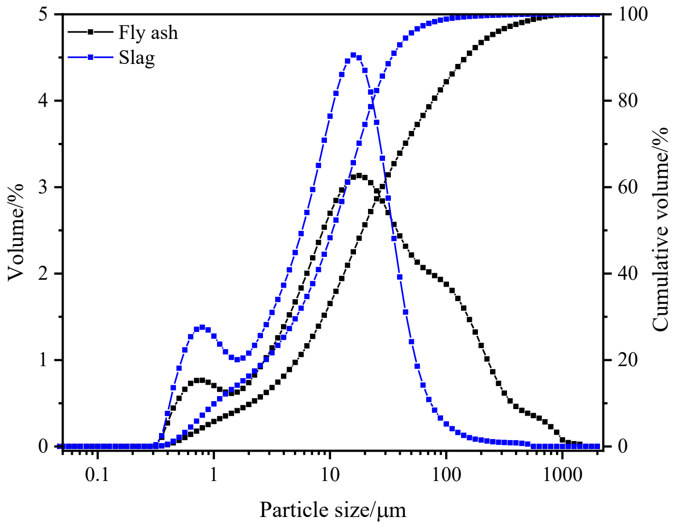

Fig.1. The size distribution of fly ash and slag

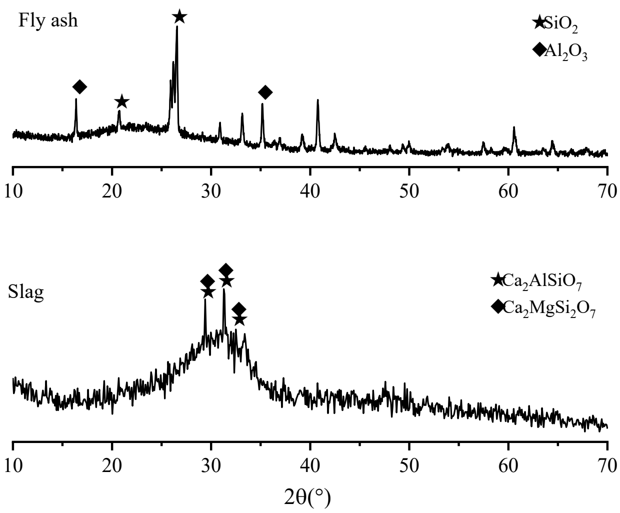

Fig.2. XRD patterns of fly ash and slag

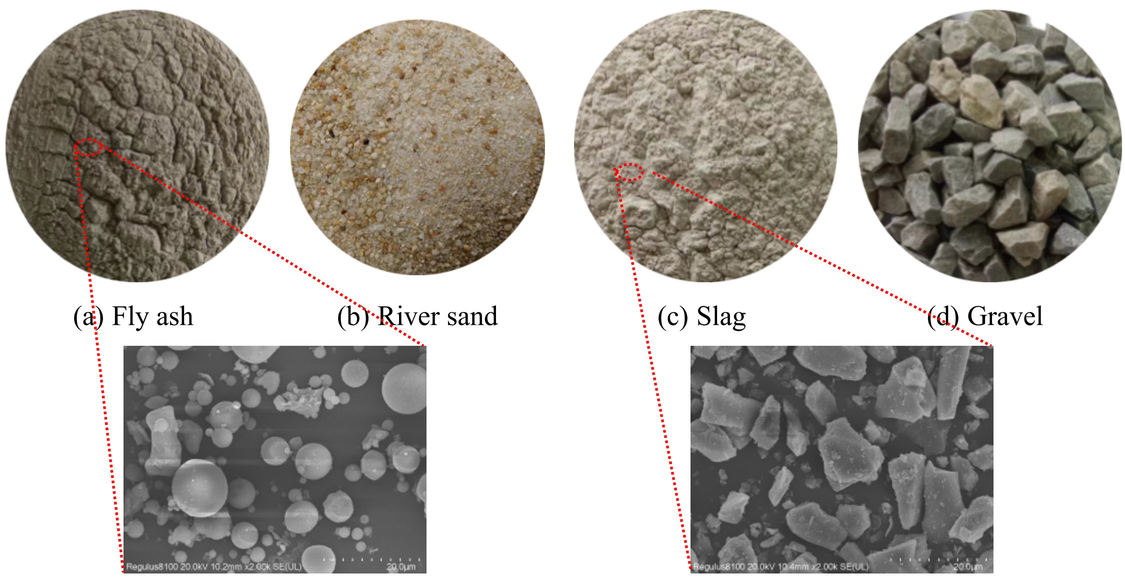

Fig.3. Raw materials and its SEM images

2.2 Mix design and sustained high temperature test

Considering the fly ash-slag mass ratios (1:0, 3:1, 1:1, 1:3, and 0:1), alkali activator modulus (0.5, 1.0, 1.5, and 2.0, molar ratio of SiO_2/Na_2O), and Na_2O concentration (4%, 6% and 8%, the mass ratio of Na_2O to the total mass of precursor) factors, ten groups of tests are designed, and the specific mix proportions are shown in Table 2. The number S0-1.5-6 indicates that the slag content is 0% (fly ash-slag mass ratio is 1:0), the activator modulus is 1.5, and the Na_2O concentration is 6%. Fig.4 is the schematic diagram of the preparation process of AAFS concrete. According to the alkali activator parameters in Table 2, prepare the alkali activator solution 24 hours prior to use to ensure it cools to room temperature by the time of application, adjusting the water addition to achieve a liquid-to-solid (L/S) ratio of 0.4. In accordance with the GB/T 50080 standard, dry-mix fly ash, slag, sand, and ordinary crushed stone for 3 minutes until thoroughly blended. Once mixed evenly, pour the mixture into the alkali activator solution and stir for an additional 3 minutes. Pour the freshly prepared concrete paste into 50mm x 50mm x 50mm cubes, and vibrate on a shaking table for 1 minute to ensure thorough compaction of the concrete, minimizing pore formation and reducing the risk of cracks due to shrinkage and internal stresses. Subsequently, cover the cubes with plastic wrap and transfer them to a standard curing room (temperature = 20±2°C, relative humidity = 95%±1%) for 1d. After this initial curing period, remove the molds and continue to store the samples in the standard curing room until the designated test age, to prevent drying cracks caused by excessive evaporation of moisture.

The sample with standard curing for 27d is taken out and dried at room temperature (RT) for 1d to accelerate the evaporation of apparent macropore free-water and weaken the effect of heating on accelerating vapor hydration. The sustained high-temperature tests are carried out in a high-temperature drying oven. The temperature levels are set at 60°C, 100°C, 150°C and 200°C respectively, and the duration is set to 3d, 7d, 28d, 60d, and 90d. The sustained high-temperature samples are 80 test blocks in each group.

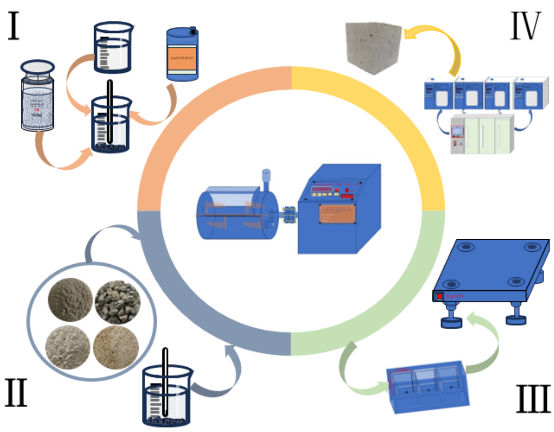

Fig.4 Schematic diagram of the preparation process of AAFS concrete

Table 2. Special mix proportions of AAFS concrete kg/m^3

Sample No.	Fly ash	Slag	Sand	Crushed stone	Alkali activator modulus	Na_2O concentration	L/S ratio
S0-1.5-6	560	0	565	1050	1.5	6%	0.4
S25-1.5-6	420	140	565	1050	1.5	6%	0.4
S50-1.5-6	280	280	565	1050	1.5	6%	0.4
S75-1.5-6	140	420	565	1050	1.5	6%	0.4
S100-1.5-6	0	560	565	1050	1.5	6%	0.4
S50-1.5-4	280	280	565	1050	1.5	4%	0.4
S50-1.5-8	280	280	565	1050	1.5	8%	0.4
S50-0.5-6	280	280	565	1050	0.5	6%	0.4
S50-1.0-6	280	280	565	1050	1.0	6%	0.4
S50-2.0-6	280	280	565	1050	2.0	6%	0.4

2.3 Characterization methods

2.3.1. Compressive strength tests

The WDW 300 micro-controlled electronic universal testing machine is used to test the compressive strength, and the test speed is 0.5kN/s. Three samples are tested in each group, and the average value of the three samples is used as the final compressive strength value.

2.3.2. Mass loss rate

The high-precision electronic scale (accurate value 0.001g) is selected for the mass-loss tests, each group tests three samples. Before the high-temperature tests, the sample is numbered and weighed as the initial mass, which is recorded as M_0; Subsequently, the sample was subjected to high-temperature treatment and was cured at temperatures such as 60℃, 100℃, 150℃, and 200℃ for durations of 3d, 7d, 28d, 60d, and 90d.The quality of the sample after high-temperature treatment was examined is recorded as M_t. The mass loss rate W is calculated as:

$$W=(M_t-M_0)/M_0\times 100\% \quad (1)$$

2.3.3. X-CT tests

Bruker SKYSCAN1272 high-resolution micro-CT scanner is selected, and the X-ray source is the high-intensity microfocal spotlight source. The sample size for the X-CT test is 50mm×50mm×50mm cube. The acceleration voltage is 250kV, and the acceleration current is 150μA. About 1300 projections are scanned in each sample, and the acquisition time of each projection is about 0.14s. The cross-section slice of AAFS concrete is shown in Fig.5. According to the different gray values of each phase, the material with higher density appears brighter in the image, and the cracks and pores are the darkest areas. The detector is a flat panel detector with a 2000×2000 pixel array. Voxel size of 39.8μm×39.8μm×39.8μm, horizontal and axial voxel sizes are equal. The derived format is "16-bit tiff ", and the grayscale range is 0~65535.

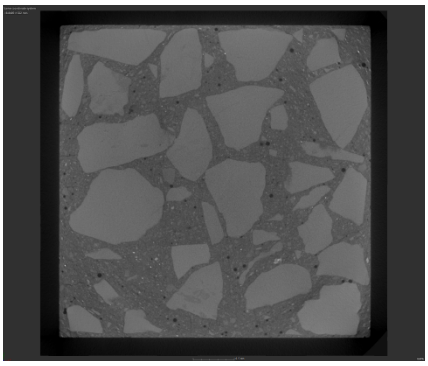

Fig.5. AAFS concrete cross-section slice diagram based on X-CT scanning

2.3.4. X-CT image pre-processing

In X-CT images, the gray data value is calculated based on the X-ray attenuation function, X-ray energy, and the density and composition of the imaged material. In general, the gray-scale data value in the periphery of the CT image is higher than the center, which is caused by the difference in X-ray energy absorption. This phenomenon is called "beam hardening" [31], which interferes with the distinction between pixels representing mesoscopic pores and cracks. Each image pixel is assigned a 16-bit gray value, in which the low value represents the hole and crack phases, and the high value represents the dense solid phases [32]. To separate low-value pixels (pores and cracks) from high-value pixels (solid mortar and coarse aggregate), Otsu-thresholding is used for image segmentation [33]. The threshold method of Otsu-thresholding gray histogram can automatically determine the appropriate threshold, convert the gray image to the threshold of binary image, and determine the optimal threshold pixel value according to the variance minimization of the two types of pixel groups. Once the threshold T is determined, the pixel value less than T is assumed to be air space, and the pixel value greater than T is entities. Due to the gray value of X-CT noise points being close to the sample pores and cracks, when the threshold is given by Otsu-thresholding, a small air space of several pixels is observed in the aggregate, which may be caused by X-CT noise points. If the threshold is adjusted, the error of pore analysis will increase, so appropriate median filtering or algorithm is used to eliminate noise points [34,35] to obtain better local and global features.

Based on the X-CT images, the meso-structure of AAFS concrete is reconstructed using the visualization image analysis software Avizo. The preprocessing process is shown in Fig.6. Part (I) shows the three-dimensional reconstruction model of AASF concrete. To more effectively analyze the internal phase distribution of concrete and avoid the edge effect caused by demoulding during sample preparation [36], Volumes of interest (VOI, 36mm×36mm×36mm) excluding sample boundaries are extracted from the 50mm×50mm×50mm cube of the original X-CT image. Part (II) shows the preprocessing of VOI slices. Firstly, the Avizo colormap module is used to improve the brightness of the original X-CT image, so that the cracks, aggregates, pores, and ITZ on the slice can be clearly observed. Secondly, the Otsu-threshold method is used for image segmentation. After setting the threshold, the darker pixels are opened to highlight the air phase, while other pixels are closed to represent the solid phase, and the effect of noise points is removed by median filtering 3×3 pixels and Avizo Non-local means algorithm. At the meso-scale, pores, cracks, aggregates, and ITZ are regarded as anisotropy. Finally, the visual three-dimensional models of each phase are reconstructed according to the Otsu-thresholding and deep learning module.

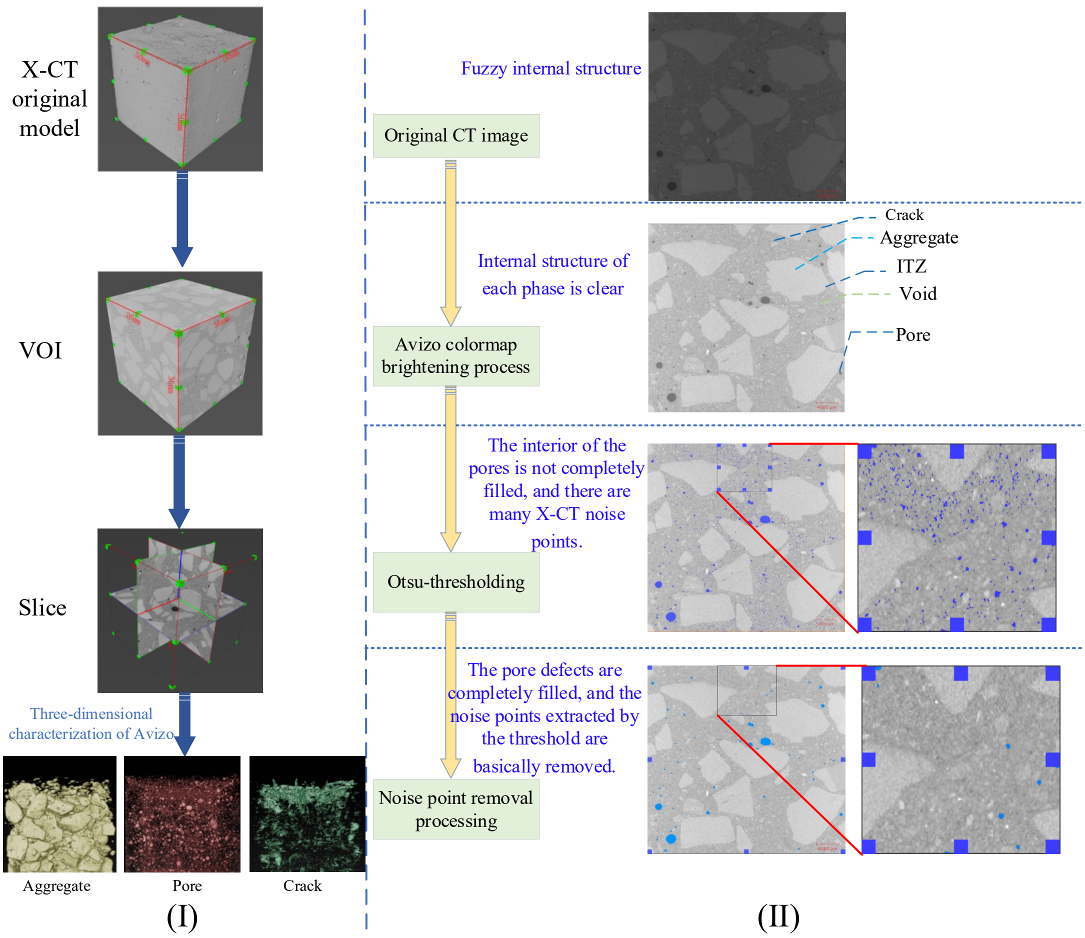

Fig.6. X-CT images preprocessing process

2.3.5. MIP tests

The AAFS concrete is broken and cored, and the coarse aggregate is removed. The granular sample of about 1cm is selected to terminate hydration with isopropanol for 48h, then low-temperature vacuum drying for 24h. AutoPore V9500 Automatic mercury porosimeter is selected, the maximum mercury pressure is 228MPa, and the continuous test is carried out in the range of 5nm~275μm. The cumulative pore volume and incremental pore volume curves of the samples are obtained.

2.3.6. SEM tests

The AAFS concrete is broken and cored, and the granular sample containing aggregate is selected to terminate the hydration with isopropanol for 48h, then low-temperature vacuum drying for 24h. The Japanese S-4800 field emission scanning electron microscope is selected, the acceleration power supply is 20kV, the current is 10nA, and the magnification is 2000 times. The morphologies of the mortar and ITZ region are tested. Gold spraying is performed before the test.

3. Results and discussions

3.1. Compressive strength analysis

Compressive strength is the most important index to evaluate the macroscopic mechanical properties of concrete. Fig.7 shows the compressive strength of AAFS concrete. Fig.7(a)~(e) is the fly ash-slag mass ratio factors. S0-1.5-6 shows different changes from other groups. The compressive strength of different temperature levels and duration are higher than that of 28 days of standard curing (0d in Fig.7). With the increase of duration, the compressive strength of AAFS concrete at each temperature level increases first and then decreases, and has the maximum compressive strength at sustained high temperature 28d. With the increase in temperature levels, the compressive strength of 3d, 7d, 28d, and 60d increase. However, its 90d compressive strength reaches the maximum at 150℃. After adding slag (Fig.7(b)~(e)), the 3d compressive strength decreases at all temperature levels. The maximum decrease in compressive strength is observed at 60°C, mainly due to internal micro-cracks caused by water loss (see Fig.11(b) and Fig.24(b)). Subsequently, with the increase in duration, the compressive strength of AAFS concrete increases first and then decreases at each temperature level. With the increase in temperature levels, the compressive strength of S25-1.5-6 and S50-1.5-6 samples increase at 3d, 7d, and 28d, and the maximum compressive strength is obtained at 200°C. The maximum compressive strength for the duration of 60d and 90d is obtained at 150°C. The compressive strength of S75-1.5-6 and S100-1.5-6 samples increases first and then decreases. The maximum compressive strength is obtained at 150°C for the duration of 3d, 7d, and 28d, and at 100°C for 90d. Overall, with the increase of slag content and duration, the temperature level of obtaining the maximum compressive strength decreases. The compressive strength of the S0-1.5-6 sample after the duration of 90d is still higher than that of RT, showing excellent sustained high-temperature resistance, but the compressive strength is low.

Fig.7(c), (f) and (g) is the Na_2O concentration factors. The compressive strength of the three groups of samples decreases first, then increases, and then decreases. The compressive strength decreases at duration for 3d, and the maximum compressive strength is obtained at 28d. The samples with 4% and 6% Na_2O concentration obtained the maximum compressive strength at 150°C, and the samples with 8% Na_2O concentration obtained the maximum value at 100°C. That is, the higher the Na_2O concentration, the lower the temperature level to obtain the maximum compressive strength, and the Na_2O concentration should be reduced when the AAFS concrete is used in a long-term thermal environment.

Fig.7(c) and (h)~(j) is the alkali activator modulus factors. The compressive strength of S50-0.5-6 and S50-1.0-6 samples increases first and then decreases at each temperature level, which is higher than that of 0d, showing excellent long-term high-temperature resistance. The compressive strength of the S50-2.0-6 sample shows a similar change rule to that of the S50-1.5-6 sample. The compressive strength of S50-2.0-6 samples after sustained high temperature is lower than that of 0d. That is, the alkali-activator modulus should be reduced when AAFS concrete is used in a long-term thermal environment.

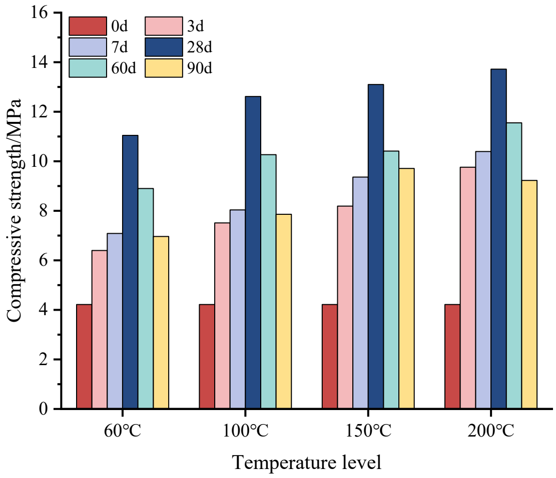

(a) S0-1.5-6

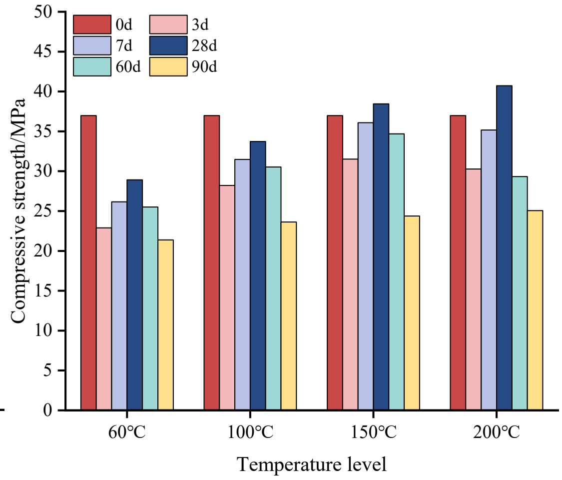

(b) S25-1.5-6

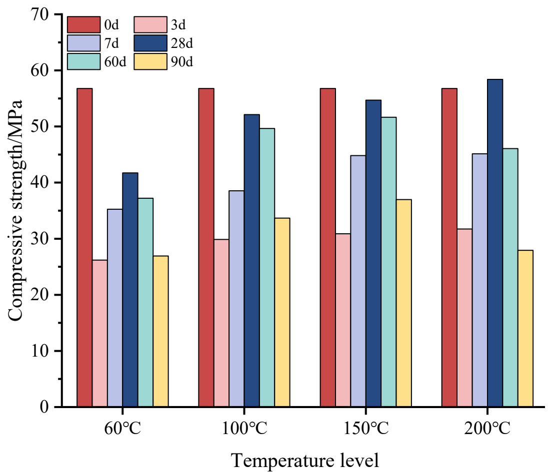

(c) S50-1.5-6

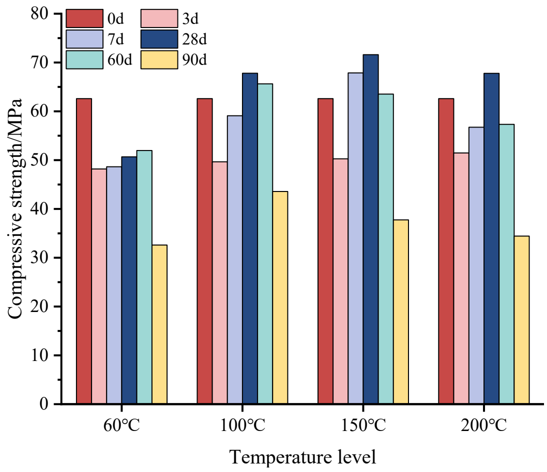

(d) S75-1.5-6

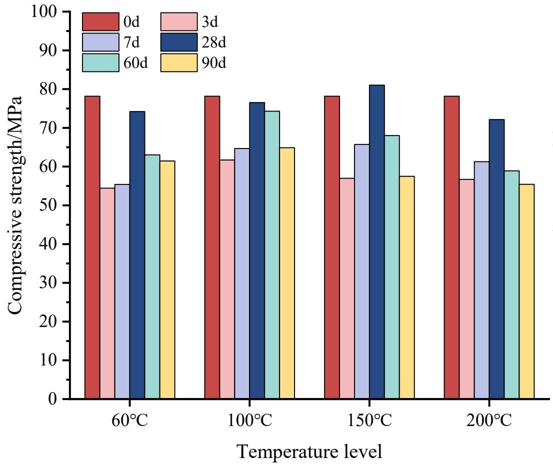

(e) S100-1.5-6

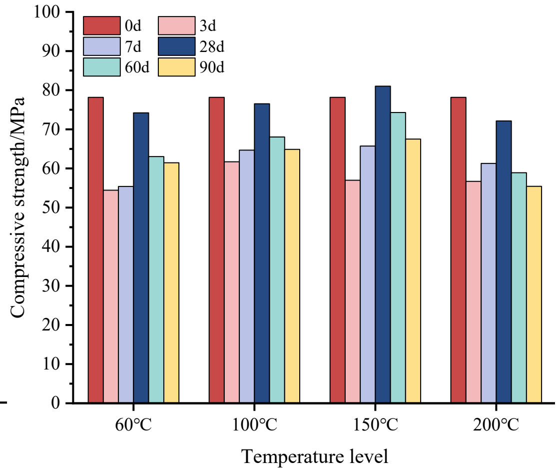

(f) S50-1.5-4

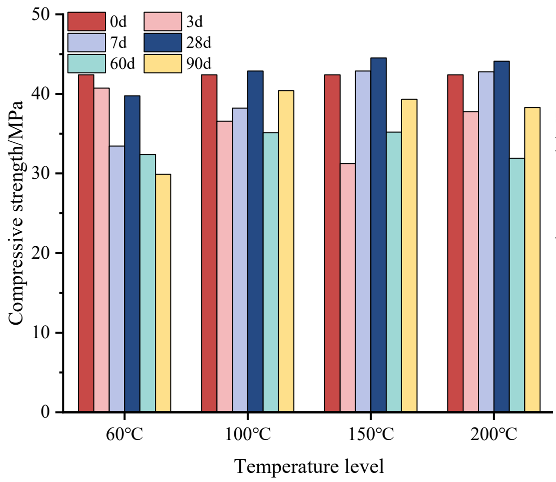

(g) S50-1.5-8

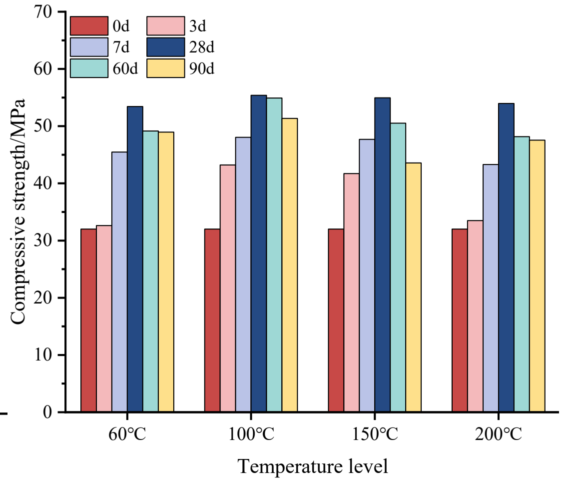

(h) S50-0.5-6

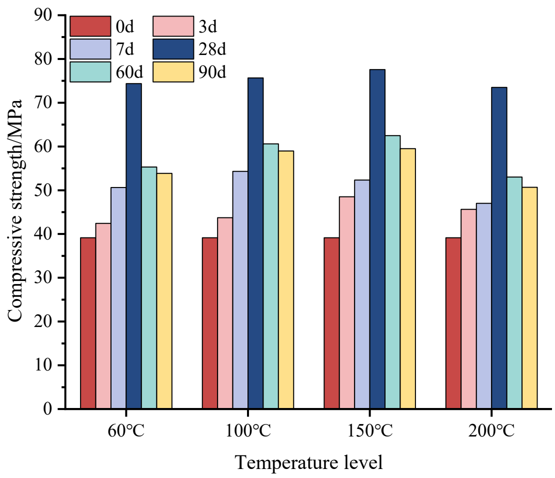

(I) S50-1.0-6

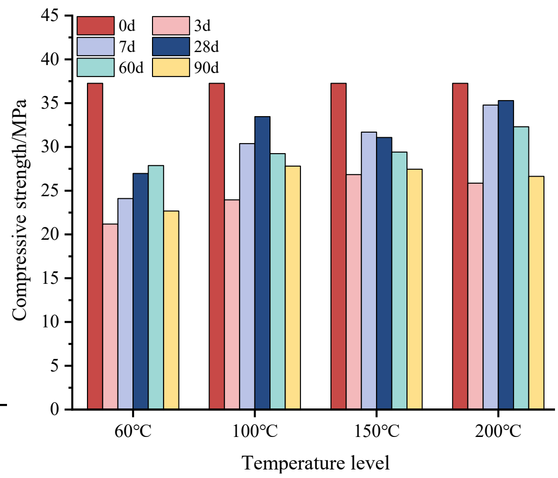

(J) S50-2.0-6

Fig.7. Compressive strength results of AAFS sample

3.2 Mass loss rate analysis

Under sustained high temperatures, free water loss, interphase water loss, phase recombination, and internal damage accumulation occur in AAFS concrete, and the crystal morphology of hydration products is greatly affected. It is of great significance to obtain the mass change of AAFS concrete after sustained high temperatures for analyzing the mechanism of performance evolution. Fig.8 shows the mass loss rate of AAFS concrete. Fig.8(a)~(e) is the fly ash-slag mass ratio factors. The mass loss rate of the five groups of samples at 150°C and 200°C show the same trend, and all reached a constant at duration for 3d. The mass loss rates at 200°C for 90d are 8.99%, 8.94%, 8.88%, 8.87%, and 9.04%, respectively, and there was no significant difference. When the temperature level is 100°C, the mass loss rate of the five groups of samples is constant at 7d, and the mass loss rates at 90d are 8.27%, 7.72%, 7.49%, 7.02%, and 6.95%, respectively. With the increase of slag content, the mass loss rate decreases at the same duration. The mass loss rate curves of the five groups of samples at 60°C show significant differences. With the increase in slag content, the time for the mass loss rate to reach a constant increases, and the final mass loss rate decreases. The main hydration product of the S0-1.5-6 sample is the N-A-S-H gel, and there is almost no calcium-containing gel phase. The mass loss rate is constant in the 3d~7d, and the mass loss rate difference at four temperature levels is less than 1% (see Fig.8(a)), indicating that the water loss of N-A-S-H gel is rapid. With the increase in slag content, the amount of C-S-H and C-A-S-H gels formation and the proportion increase [37]. The mass loss rate of 90d at 100°C decreases with the increase of slag content, which indicates that some C-S-H and C-A-S-H gels bound water is stable at 100°C. The mass loss rate at 60°C tends to be constant at 60d (see Fig.7(d) and (e)), indicating that the water loss of C-S-H and C-A-S-H gel phases at 60°C is continuous. With the increase in slag content, the greater the difference between the mass loss rate at 60℃ and 100℃ and the mass loss rate at 200℃ (the greater the distance between the curves), which can be clearly explained that the bound water of the calcium-containing gel phase is more stable than the sodium-containing gel phase at 60℃ and 100℃. This is an interesting result.

Fig.8(c), (f) and (g) is the Na_2O concentration factors. The three groups of samples show the same change rule at 100°C, 150°C, and 200°C, and there is no significant difference in mass loss rate. At 60℃, when Na_2O concentration is 4% and 8%, the mass loss rate tends to be stable for 7d. According to the compressive strength test results, the maximum compressive strength is obtained at 6% Na_2O concentration, and more C-A-H and C-A-S-H gels may be generated. Fig.8(c) and (h)~(j) is the alkali activator modulus factors. The S50-2.0-6 sample shows a large difference from the other three groups at 60℃, which may be related to its low compressive strength.

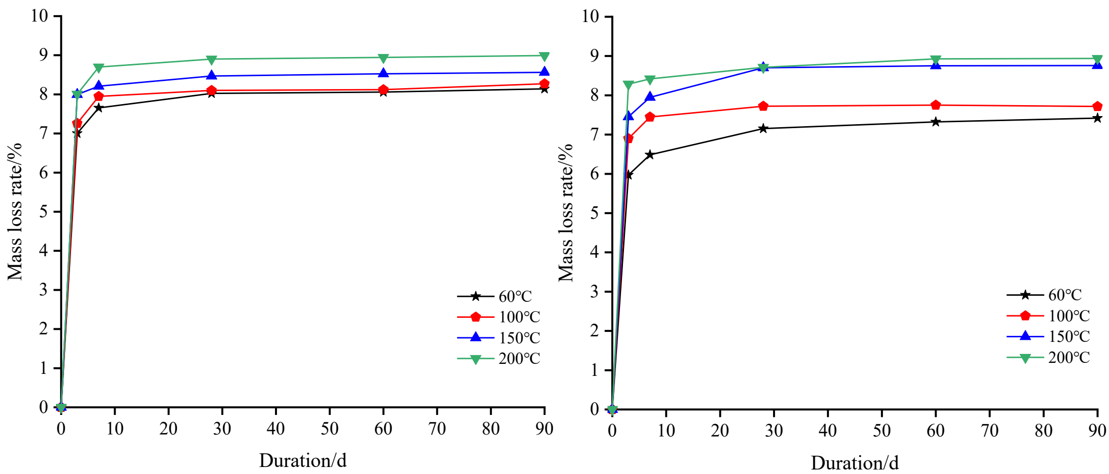

(a) S0-1.5-6 (b) S25-1.5-6

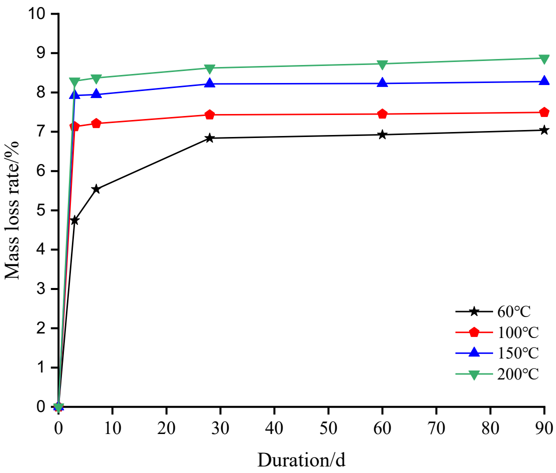

(c) S50-1.5-6

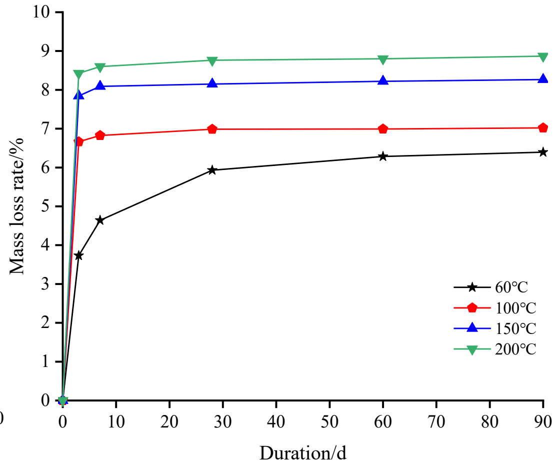

(d) S75-1.5-6

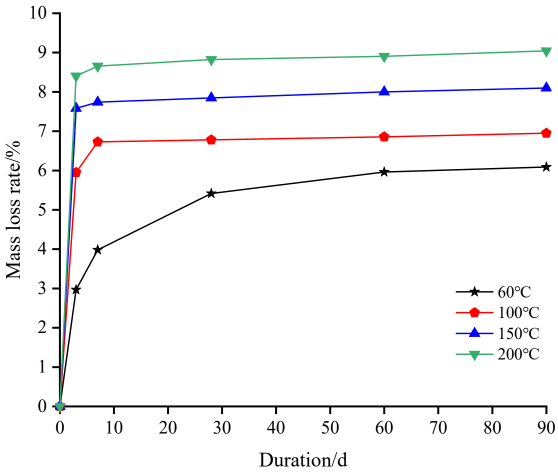

(e) S100-1.5-6

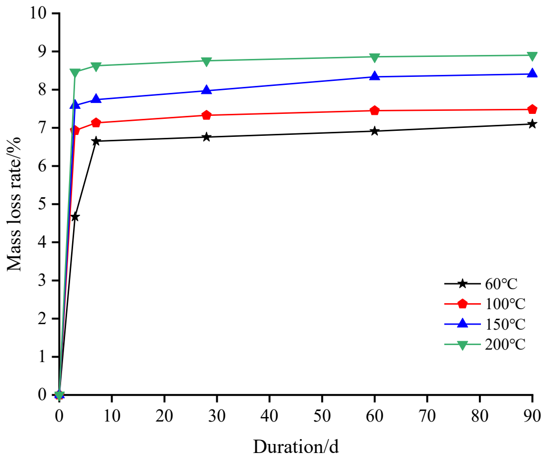

(f) S50-1.5-4

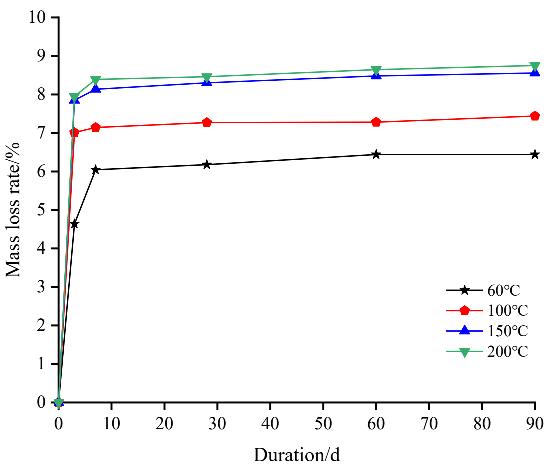

(g) S50-1.5-8

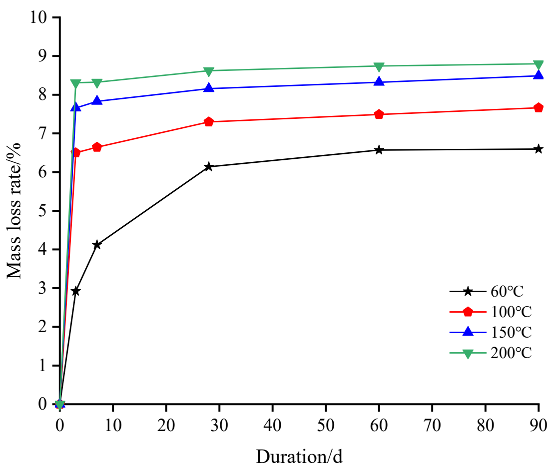

(h) S50-0.5-6

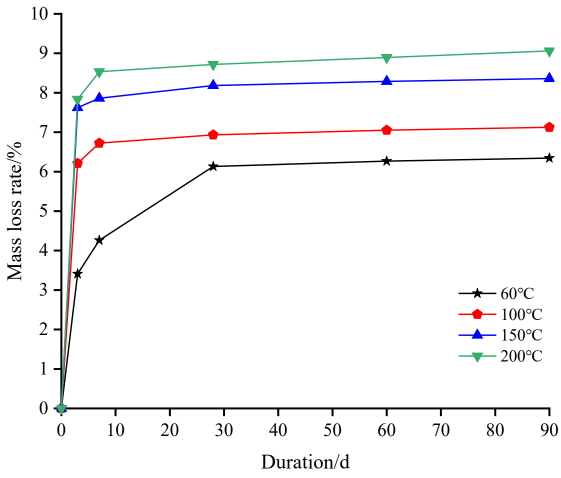

(i) S50-1.0-6

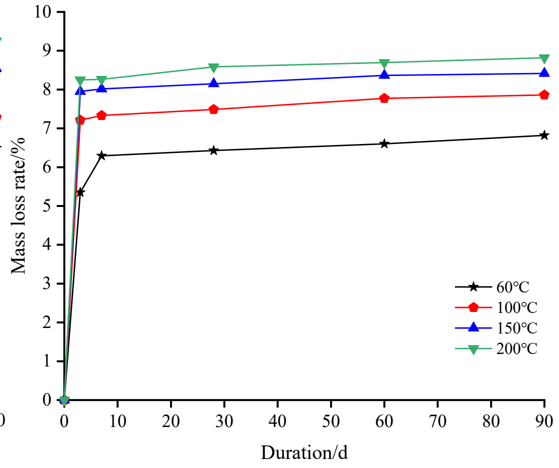

(j) S50-2.0-6

Fig.8. Mass loss rates of AAFS concrete

3.3 X-CT result analysis

3.3.1 Initial scan and crack segmentation

Fig.9 shows the X-CT images of AAFS concrete with different fly ash-slag ratios at 200℃ for 28d. No obvious micro-cracks are observed in the S0-1.5-6 sample; with the increase in slag content, different micro-cracks begin to appear between the mortar and the aggregate. S25-1.5-6 sample can see a small number of vertical surface cracks and radial cracks between adjacent aggregates; Tangential cracks are observed in the ITZ in the S50-1.5-6 and S75-1.5-6 samples, and the number of radial cracks increases and the crack width increases. Long cracks are observed in the S100-1.5-6 sample, the number of radial micro-cracks increases significantly, and ITZ tangential cracks are observed. With the increase in slag content, the number and length of radial cracks increase significantly, tangential cracks appear, and the crack width is about 0.1mm~0.6mm.

Fig.10 shows the X-CT images of S50-1.5-6 samples with different duration at 150℃. The morphology of mortar becomes rough after continuous high temperatures, which is related to the deformation of the gel phases. No obvious micro-cracks are observed in the samples with sustained high temperatures for 0d. Large slender radial cracks appear in the AAFS concrete with sustained high temperature for 3d, and the number of micro-cracks decreases when the duration is 7d. The number and length of micro-cracks in the sample are reduced at duration for 28d, and the internal structure is dense. After that, with the increase in duration, the number and width of cracks increase. Especially when the duration is 90d, the cracks are all over the surface of the whole sample, and tangential cracks appear at the ITZ, and the number and width of cracks increase significantly. Fig.11 shows the X-CT images of S50-1.5-6 samples with different temperature level at 28d. At 60°C, vertical surface cracks appear inside the sample, and obvious radial cracks occur between aggregates. At 100°C, 150°C, and 200°C, the internal cracks of the sample decrease significantly, and only a few cracks occur in the ITZ and around the pores, and the length and width of the cracks decrease significantly.

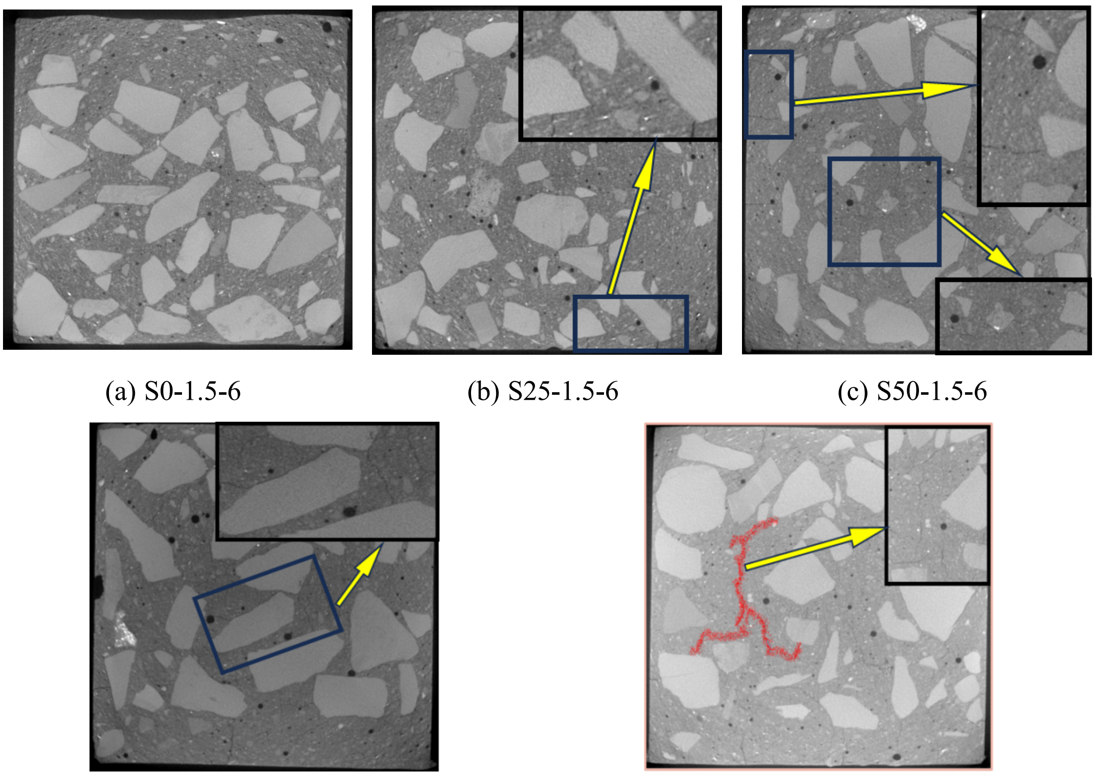

(a) S0-1.5-6 (b) S25-1.5-6 (c) S50-1.5-6

(d) S75-1.5-6 (e) S100-1.5-6

Fig.9. The X-CT images of AAFS concrete with different fly ash-slag ratios at 200°C for 28d

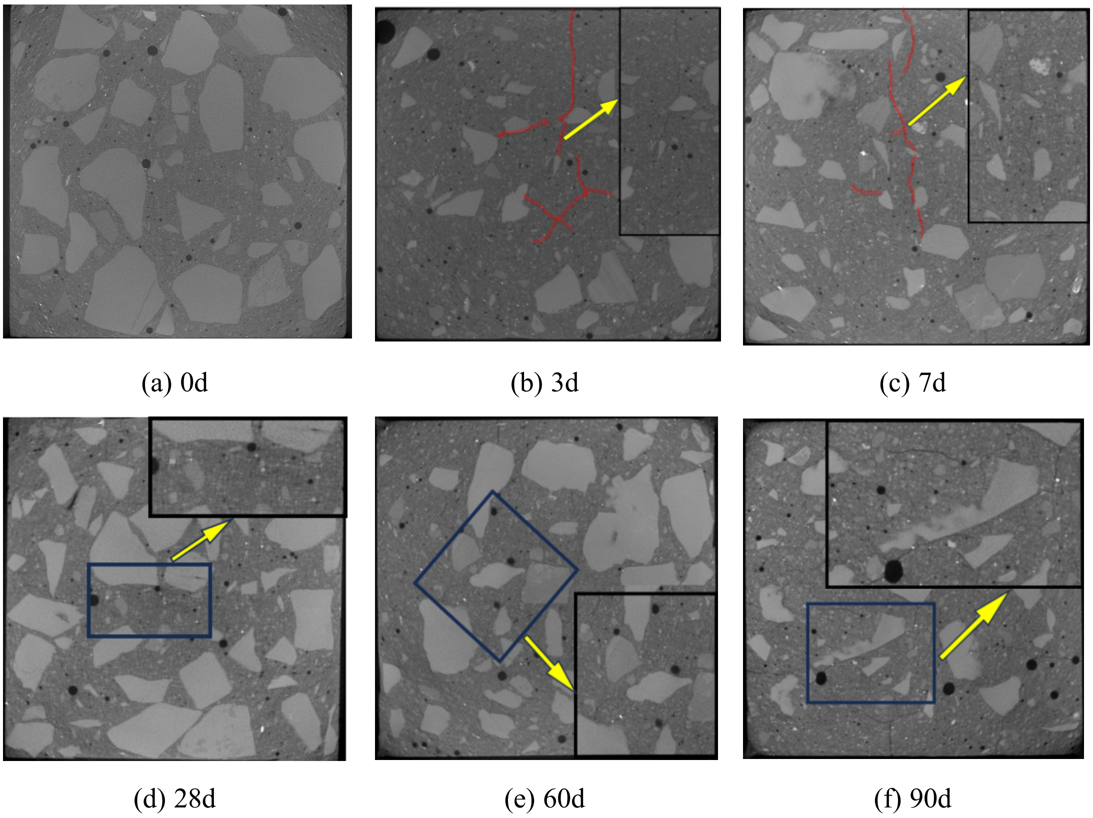

Fig.10. The X-CT images of S50-1.5-6 samples with different duration at 150℃

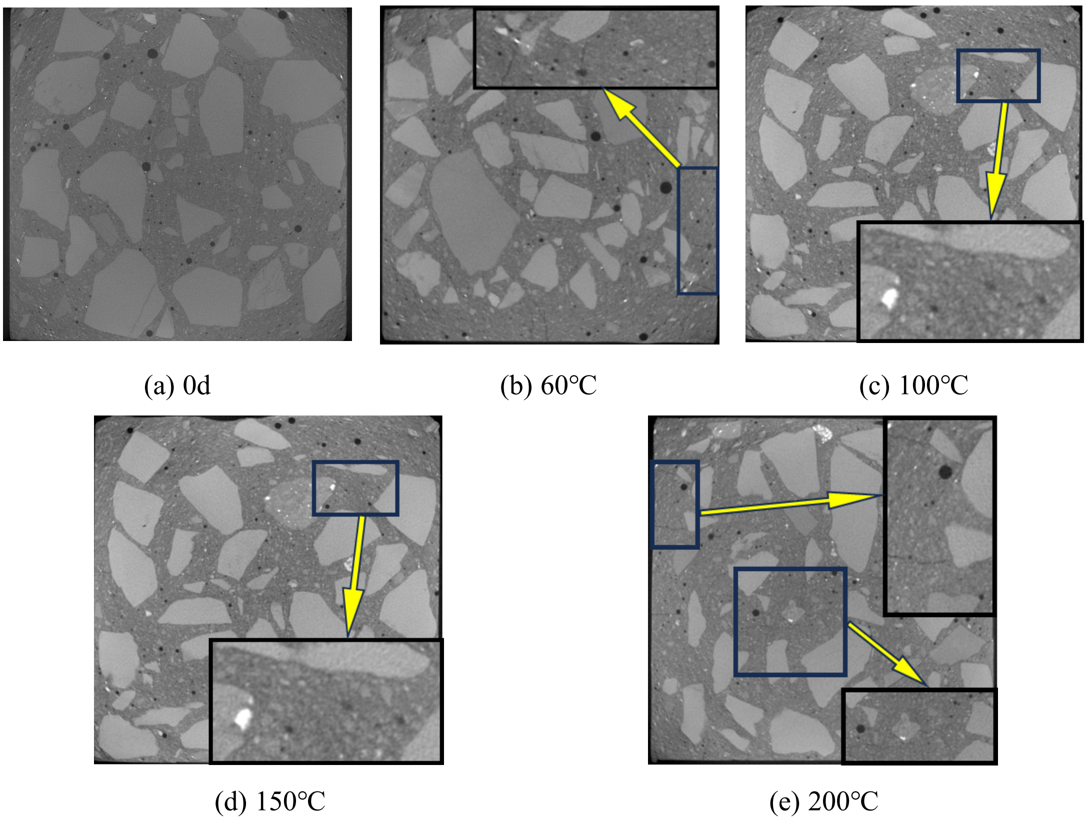

Fig.11. The X-CT images of S50-1.5-6 sample with different temperature levels for 28d

3.3.2 Three-dimensional geometry and distribution of pores

The mechanical properties of AAFS concrete depend on pore characteristics, which are closely related to the size, geometry, and volume distribution of pore defects [38,39]. Due to the small size of the sample used in this study, the results of compressive strength and mass loss rate analysis found that the steam curing environment created by water evaporation can be ignored. In Fig.9-Fig.11, the changes in micro-cracks are related to the pore structure. The rapid loss of water in the early stage, the increase of internal pore tension and micro-cracks. With the rearrangement of the gel phase, the micro-cracks and the pore structure change.

The visualization three-dimensional pore model of AAFS concrete is established based on Avizo. According to the pore geometry or volume, it is divided into four pore types: <0.3mm^3, 0.3~0.7mm^3, 0.7~1.0mm^3, and >1.0mm^3. Fig.12 shows the pores volume distributions three-dimensional visualization reconstruction of AAFS concrete with different fly ash-slag ratios at 200℃ for 28d. The pore shapes are circular, elliptical, and irregular, most of which are circular and independent of each other. It can be seen that with the increase in slag content, all kinds of pore density decrease, and most of the pores of samples are concentrated in <0.3mm^3 and >1.0mm^3. Table 3 shows the pore characteristics of AAFS concrete were obtained by X-CT, and Fig.15 shows the pore volume proportion of AAFS concrete by X-CT. With the increase in slag content, the proportion of pores in different volumes increases. When the slag content is 0%, 25%, 50%, 75%, and 100%, the pore volume ratio of the concrete samples is 2.276%, 1.567%, 1.282%, 1.010%, and 0.546%, respectively, and the pore volume decreases continuously.

Fig.13 shows the pores volume distributions three-dimensional visualization reconstruction of S50-1.5-6 samples with different duration at 150℃. After high temperatures, the pore volume increases. With the increase in duration, the total pore volume increases first, then decreases, and then increases, which is consistent with the change law of compressive strength. The pore volume change is mainly caused by $<0.3mm^3$ pores. Fig.14 shows the pores volume distributions three-dimensional visualization reconstruction of S50-1.5-6 sample with different temperature levels for 28d. The pore volume after high temperature is higher than that of room temperature curing samples. With the increase in temperature, the total porosity of the samples is RT<150°C<60°C<100°C<200°C. There is no significant difference in pore volume at 60°C, 100°C, and 150°C, however, the pore volume of $>1.0mm^3$ continues to increase, and that of $<0.3mm^3$ continues to decrease. At 200°C, the pore volume increase significantly, the pore volume of $>1mm^3$ is improved, and that of $<0.3mm^3$ increase.

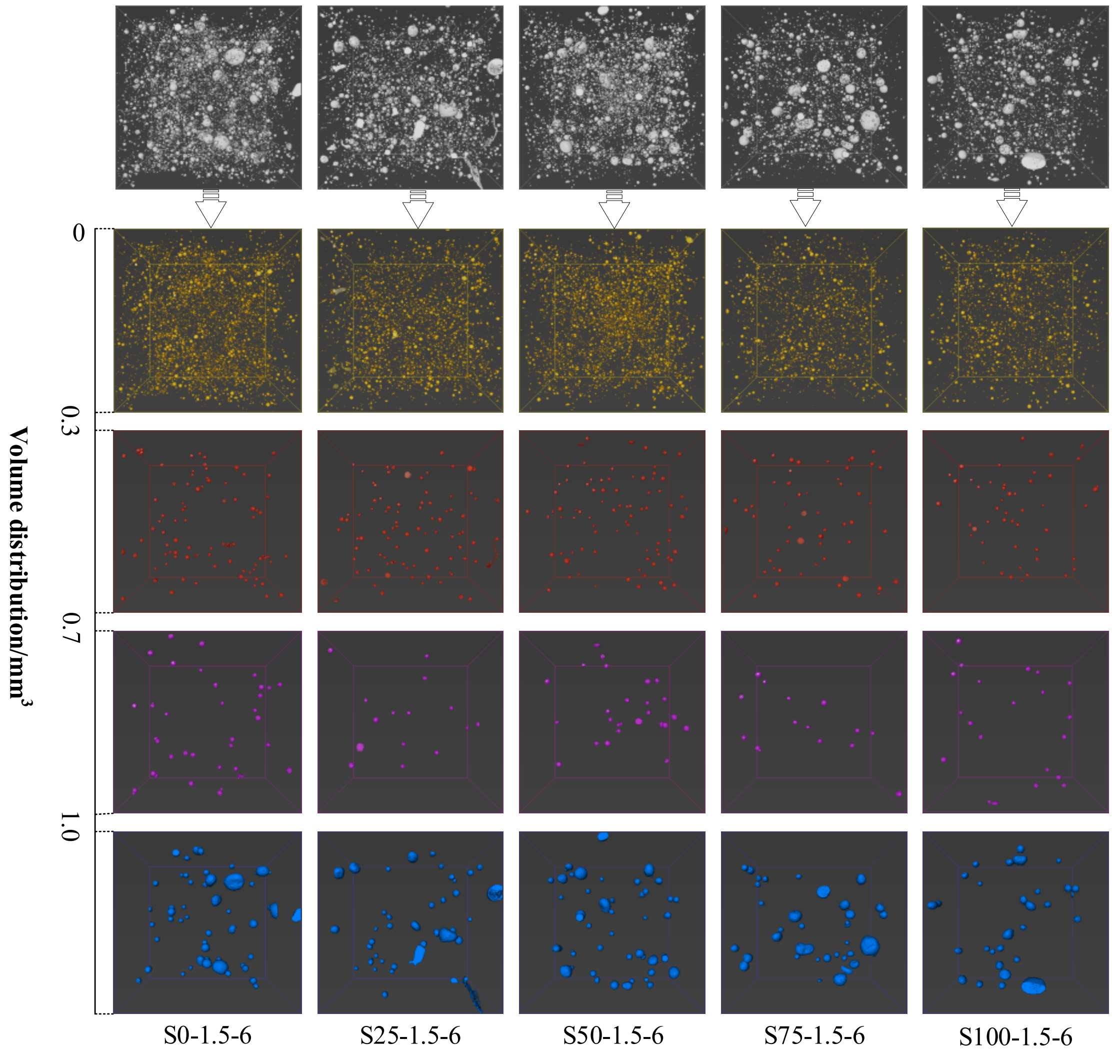

Fig.12. Pores volume distributions three-dimensional visualization reconstruction of AAFS concrete with different fly ash-slag ratios at 200°C for 28d

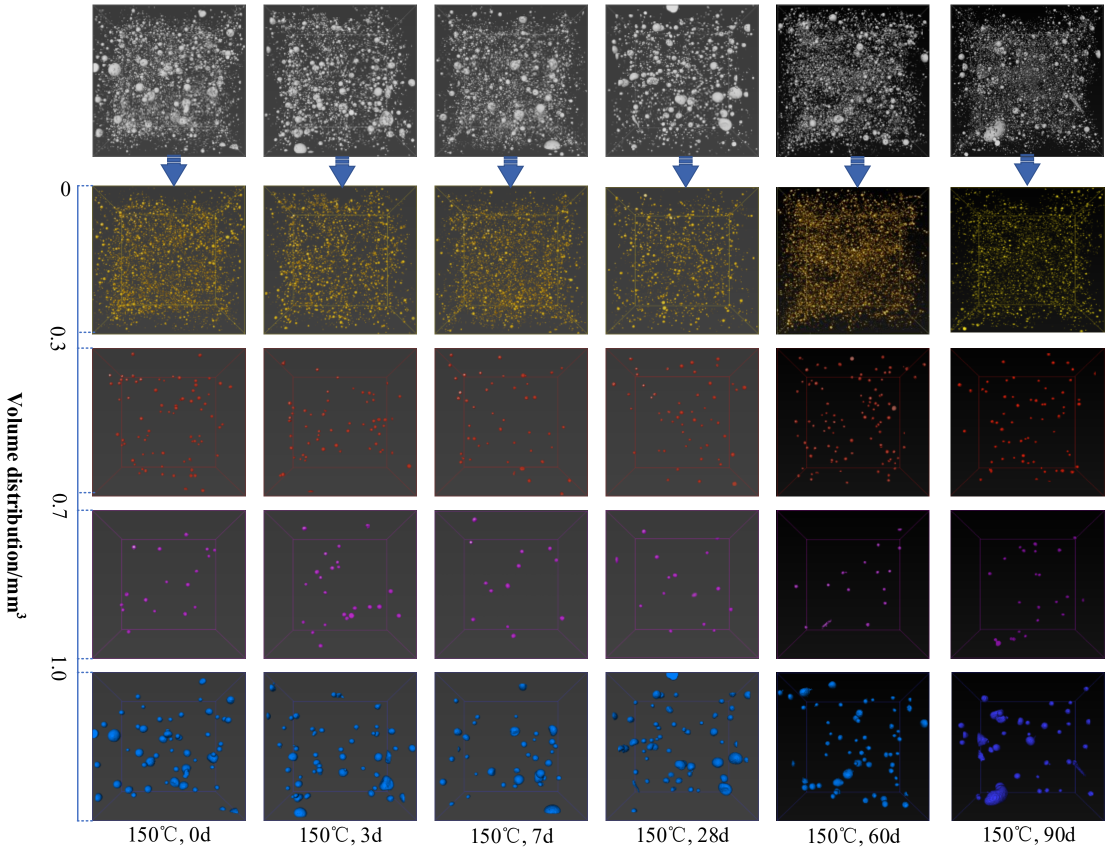

Fig.13. Pores volume distributions three-dimensional visualization reconstruction of S50-1.5-6 samples with different duration at 150°C

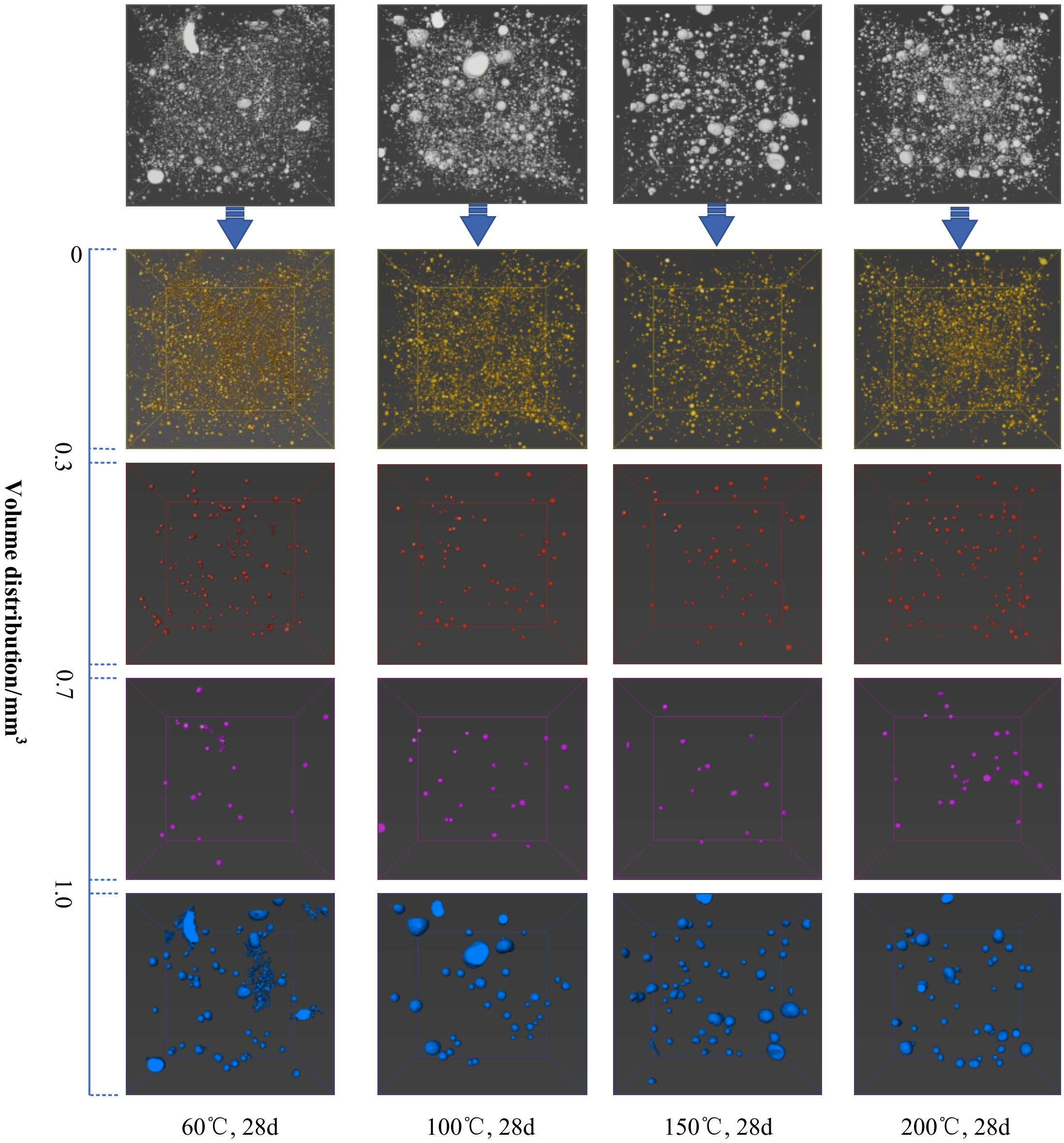

Fig.14. Pores volume distributions three-dimensional visualization reconstruction of S50-1.5-6 sample with different temperature levels for 28d

Table 3. The pore characteristics of AAFS concrete were obtained by X-CT

Sample No.	Pore distribution (%)				Pore volume /%
	<0.3mm^3	0.3-0.7mm^3	0.7-1.0mm^3	>1.0mm^3	
S0-1.5-6, 28d, 200°C	1.120	0.140	0.058	0.959	2.276
S25-1.5-6, 28d, 200°C	0.848	0.139	0.070	0.510	1.567
S50-1.5-6, 28d, 200°C	0.678	0.094	0.045	0.465	1.282
S75-1.5-6, 28d, 200°C	0.349	0.075	0.039	0.546	1.010
S100-1.5-6, 28d, 200°C	0.185	0.053	0.031	0.278	0.546

S50-1.5-6, 0d, 150°C	0.205	0.059	0.031	0.513	0.807
S50-1.5-6, 3d, 150°C	0.388	0.084	0.038	0.524	1.034
S50-1.5-6, 7d, 150°C	0.427	0.071	0.028	0.460	0.987
S50-1.5-6, 28d, 150°C	0.192	0.068	0.038	0.617	0.915
S50-1.5-6, 60d, 150°C	0.617	0.097	0.028	0.423	1.165
S50-1.5-6, 90d, 150°C	0.495	0.078	0.025	0.697	1.295
S50-1.5-6, 28d, 60°C	0.523	0.106	0.031	0.420	1.080
S50-1.5-6, 28d, 100°C	0.453	0.080	0.0417	0.526	1.101

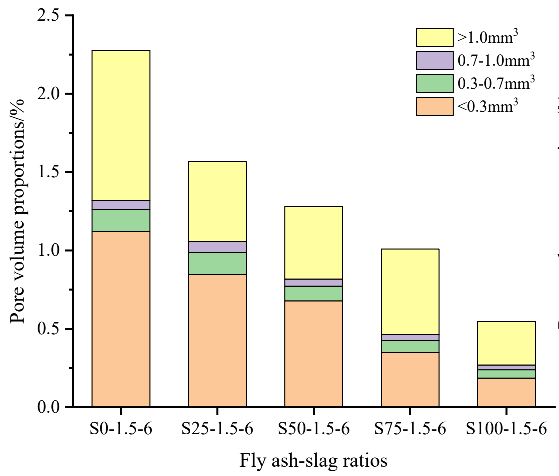

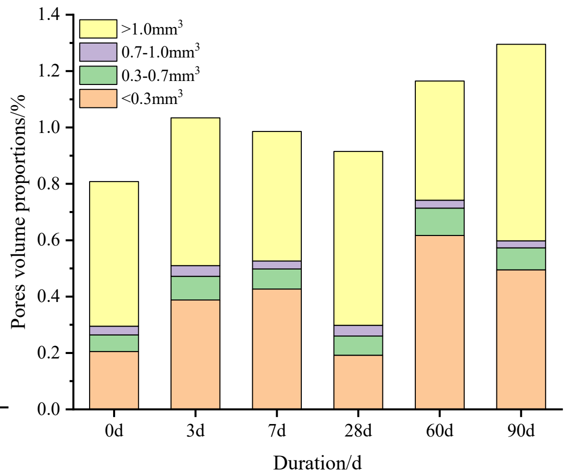

(a) Fly ash-slag ratios (b) Duration, S50-1.5-6, 150°C

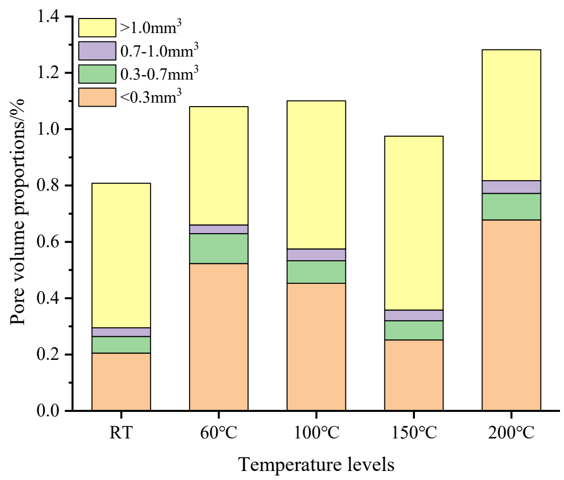

(c) Temperature levels, S50-1.5-6, 28d

Fig.15. The pore volume proportion of AAFS concrete by X-CT

3.4 MIP analysis

The voxel size used in the X-CT test is 39.8μm×39.8μm×39.8μm, and the tested pores are micron scale (diameter>39.8μm), which characterize the meso-scale pore structure. High-precision characterization of nano-scale pore changes requires MIP testing [40]. Using Hodot's pore classification method, micro-scale pore sizes are divided into gel pore(<10nm), transition pore(10nm~100nm), capillary pore(100nm~1000nm), and large pore(>1000nm) [41]. Fig.16 shows the pore size distribution of AAFS concrete with different fly ash-slag ratios at 200°C for 28d. The cumulative pore volumes of AAFS concrete with slag content of 0%, 25%, 50%, 75%, and 100% are 0.208mL/g, 0.157mL/g, 0.092mL/g, 0.067mL/g and 0.038mL/g, respectively (see Fig.16(a)). With the increase in slag content, the cumulative pore volume decreases significantly, among which the large pore volume has no significant difference, and the capillary pore volume decreases gradually. The transition pore volume reaches its maximum when the fly ash-slag mass ratio is 3:1, and then gradually decreases. The gel pore volume is very small. The pure fly ash system has a large volume of capillary pore, and the transition pore volume of the system increases after adding slag. With the increase in total pore volume, the volume of all pore types decreases.

Fig.17 shows the pore size distribution of S50-1.5-6 samples with different duration at 150°C. The cumulative pore volume increases first, then decreases, and then increases with the increase of duration, especially at 60d and 90d, the cumulative pore volume increases significantly. The gel pore and transition pore volume increase significantly at durations of 60d and 90d. There is no significant difference in capillary pore volume under different durations. The large pore volume shows the same change as the cumulative pore volume. Fig.18 shows the pore size distribution of S50-1.5-6 sample with different temperature levels for 28d. With the increase in temperature level, the cumulative pore volume first increases and then decreases, which is higher than that of RT. At 150°C, the cumulative pore volume decreases, which is consistent with the microscopic pore results of the X-CT test, indicating that the internal structure of AAFS concrete is denser than that of other temperatures after 28d at 150°C. Compared with RT samples, the capillary pore and large pore volume of AAFS concrete increase significantly under high temperatures, and there is no significant difference in the capillary pore and large pore volume among the four groups of samples at 60°C~200°C. At 60°C, part of the gel phases bound water is lost and increases the transition pore volume; At 100°C, the loss of gel phases bound water is large, which further increases the transition pore volume; At 150°C, the gel phases bound water is completely lost, with the accelerated recombination of the gel phases, the transition pore volume decreases. There is no gel pore in AAFS concrete due to the loss of gel phases bound water. At 200°C, the unstable gel phases decompose, resulting in the increase of transition pore and the appearance of gel pore. The transition pore volume first increases, then decreases, and then increases, showing the same change rule as the cumulative pore volume.

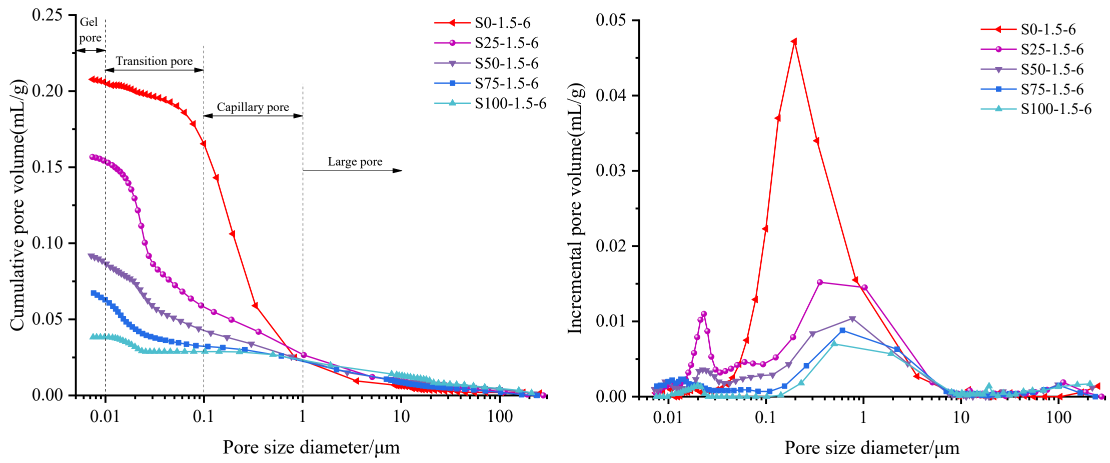

(a) Cumulative pore volume (b) Incremental pore volume

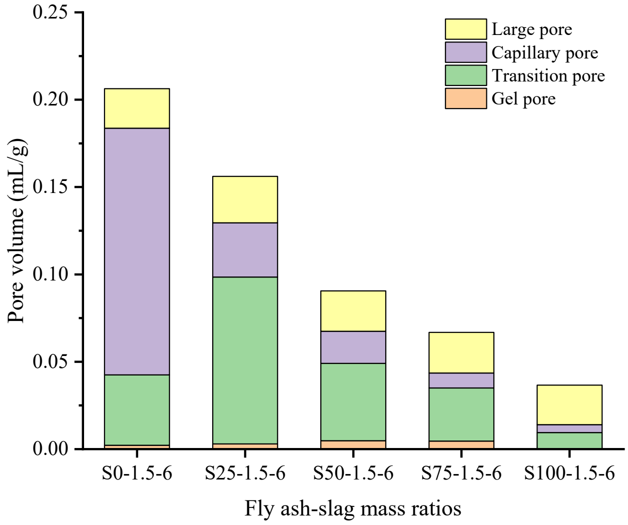

(c) Proportion of different size pores

Fig.16. The pore size distribution of AAFS concrete with different fly ash-slag ratios at 200℃ for 28d

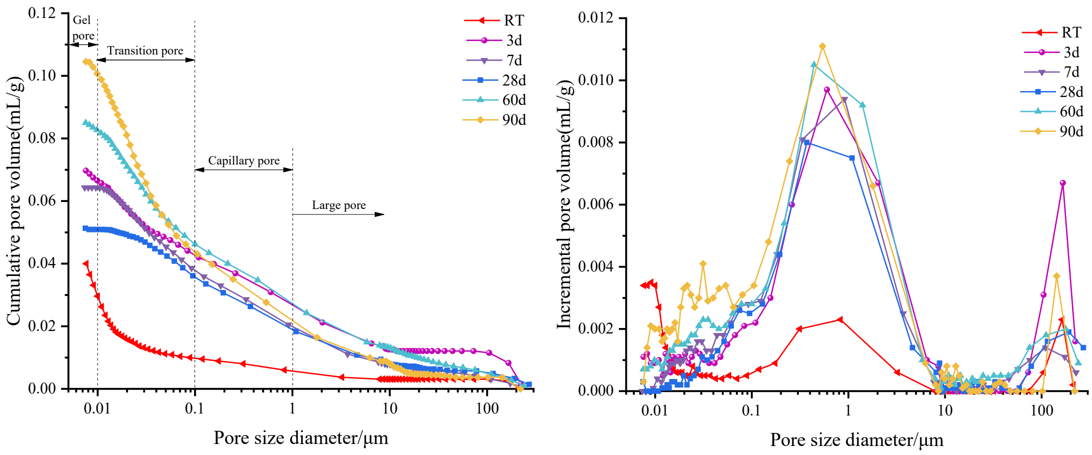

(a) Cumulative pore volume (b) Incremental pore volume

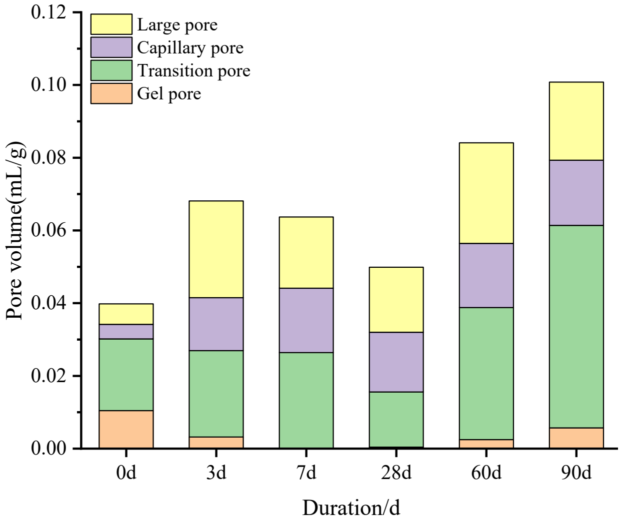

(c) Different sub-high temperature duration

Fig.17. The pore size distribution of S50-1.5-6 samples with different duration at 150°C

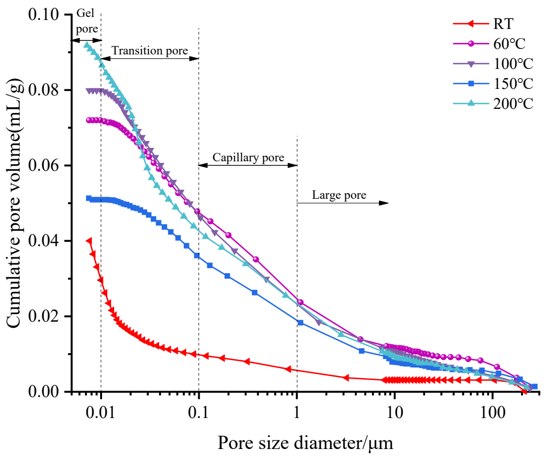

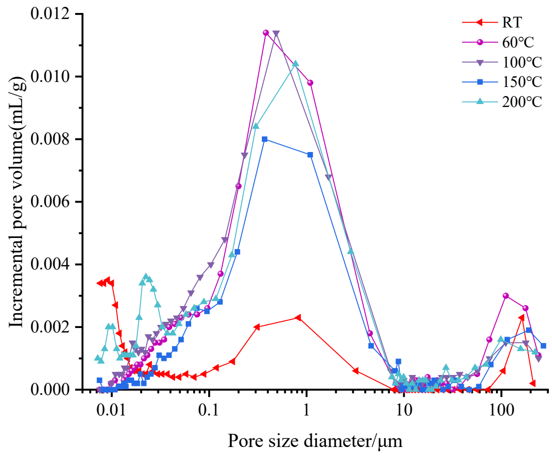

(a) Cumulative pore volume (b) Incremental pore volume

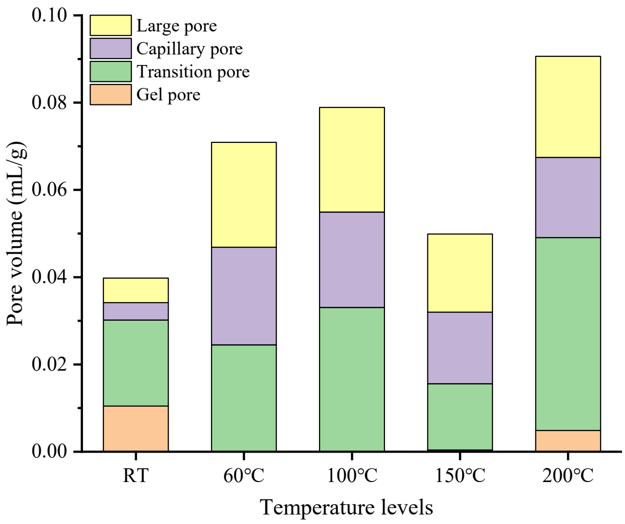

(c) Different sub-high temperature levels

Fig.18. The pore size distribution of S50-1.5-6 sample with different temperature levels for 28d

3.5 SEM analysis

3.5.1 SEM images of AAFS mortars

SEM tests are carried out on AAFS concrete, including AAFS mortar and ITZ. Fig.19 shows the SEM images of AAFS mortars with different fly ash-slag mass ratios. With the increase in slag content, the compactness of AAFS mortar increases significantly. Micro-cracks and unreacted "glass microsphere" fly ash particles are clearly seen in S0-1.5-6 and S25-1.5-6 samples, and the microstructure is loose. The unhydrated fly ash particles have a filling effect on the matrix, and the matrix is relatively continuous. The loose microstructure indicates that N-A-S-H gel phase recombination performance is poor after sustained high-temperature dehydration [17]. With the increase in slag content, due to high-temperature water loss, the real morphology of hydration products cannot be seen. Flocculent or granular hydration products agglomerate with unhydrated raw materials to form blocks, and the microstructure is obviously dense. Fig.20 shows the SEM images of AAFS mortars with different duration at 150°C. When sustained high temperatures for 3d and 7d, the surface of the sample is relatively loose, and the large polymer is decomposed into small blocks. There are many micro-cracks in the 3d sample, and the width of the micro-cracks is smaller. When the duration is 28d, 60d, and 90d, the microstructure becomes dense, the hydration products are combined into one piece, and the matrix becomes dense, which is related to the restructuring of the hydration products of the gel phases. Fig.21 shows the SEM images of AAFS mortars with different temperature levels. The flocculent C-(A)-S-H and N-A-S-H gels are observed in AAFS mortars cured at RT, 60°C, and 100°C. At 60°C and 100°C, there are many obvious microcracks. At 150°C and 200°C, the microstructure of the sample is dense, which is related to the rapid restructuring of the gel phases.

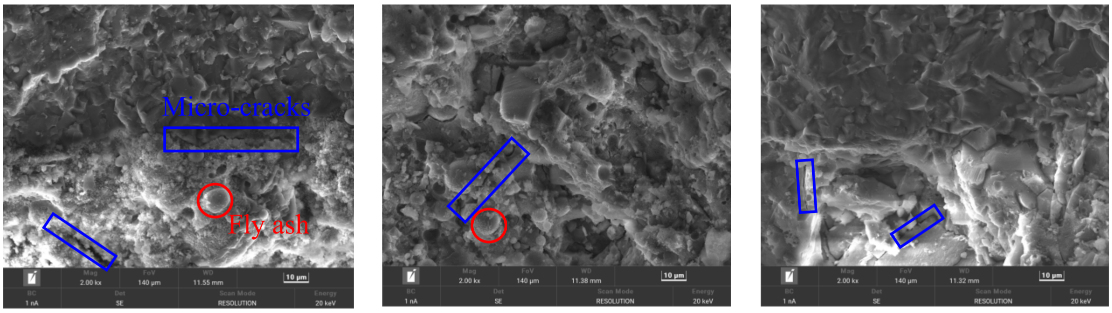

(a) S0-1.5-6, 200°C, 28d (b) S25-1.5-6, 200°C, 28d (c) S50-1.5-6, 200°C, 28d

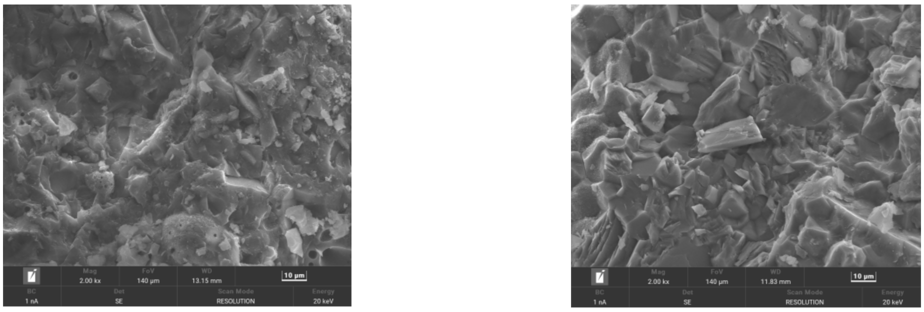

(d) S75-1.5-6, 200°C, 28d (e) S100-1.5-6, 200°C, 28d

Fig.19. SEM images of AAFS mortars with different fly ash-slag mass ratios

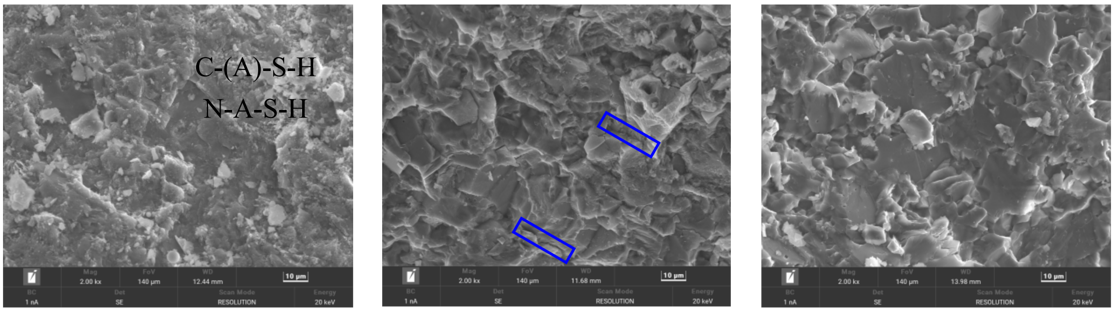

(a) S50-1.5-6, 150°C, 0d (b) S50-1.5-6, 150°C, 3d (c) S50-1.5-6, 150°C, 7d

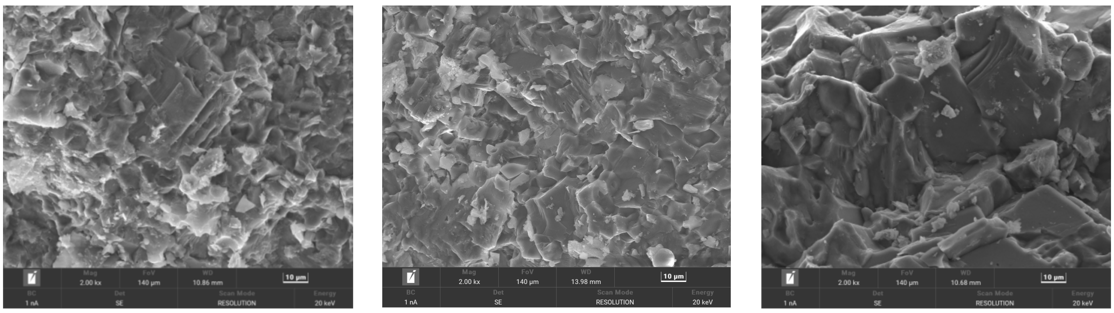

(d) S50-1.5-6, 150°C, 28d (e) S50-1.5-6, 150°C, 60d (f) S50-1.5-6, 150°C, 90d

Fig.20. SEM images of AAFS mortars with different duration

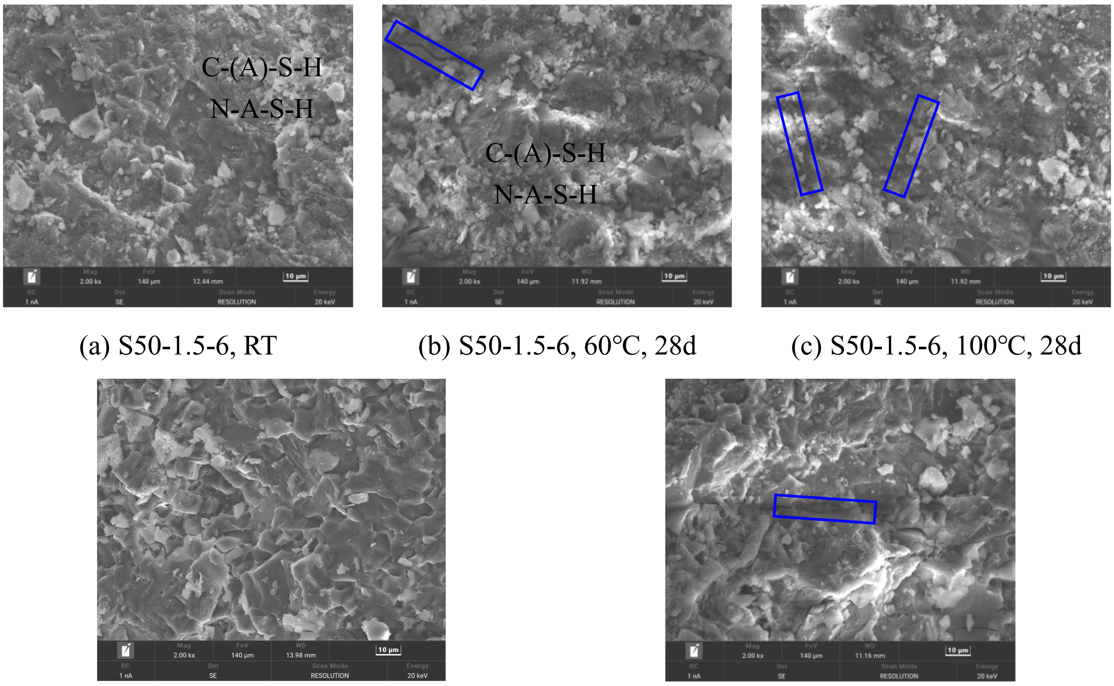

(a) S50-1.5-6, RT (b) S50-1.5-6, 60℃, 28d (c) S50-1.5-6, 100℃, 28d

(d) S50-1.5-6, 150℃, 28d (e) S50-1.5-6, 200℃, 28d

Fig.21. SEM images of AAFS mortars with different temperature levels

3.5.2 ITZ microstructure

The heterogeneity of concrete considers matrix, aggregate, and ITZ as anisotropy. Due to the "wall effect", the composition distribution and properties of ITZ are different from those of the matrix [42], and the heterogeneity of ITZ is a key factor affecting the performance of AAFS concrete. The X-CT test results show that the ITZ of AAFS concrete appears tangential or radial cracks after sustained high temperatures. The ITZ width of alkali-activated concrete is about 15-50μm [3,42], and the ITZ of AAFS concrete can be more clearly seen by SEM test. Fig.22 shows the ITZ microstructure of AAFS concrete with different fly ash-slag mass ratios by SEM tests. Due to the loose structure of the mortar, the ITZ of the S0-1.5-6 sample did not show obvious micro-cracks. After adding slag, obvious tangential and radial cracks appear in the ITZ region. With the increase in slag content, the mortar matrix in the ITZ region is more and more dense, and the tangential crack is more obvious. The radial crack of the S75-1.5-6 sample is the widest, about 1.8μm.

Fig.23 shows the ITZ microstructure of S50-1.5-6 concrete sample with different duration. The ITZ of S50-1.5-6 concrete samples at RT is relatively dense, and there are no obvious micro-cracks. After the high-temperature action of 3d and 7d, ITZ has obvious cracks, and the mortar matrix in the nearby area has cracks, which are mainly caused by the rapid water loss of the matrix. There is no obvious radial crack in the ITZ region of the sample after duration for 28d, and there are small tangential cracks in the mortar matrix, and the matrix is obviously dense. After the duration of 60d and 90d, the length and width of the radial micro-cracks in the ITZ region increase with the increase of duration, and the maximum width of the micro-cracks in the sample with sustained high temperature for 90d is about 2.6μm. The number and width of tangential micro-cracks are more than those of duration for 28d. Fig.24 shows the ITZ microstructure of S50-1.5-6 concrete sample with different temperature levels. At 60℃ and 100℃, the matrix restructuring speed is slow and the mortar matrix is relatively loose, resulting in obvious radial cracks in ITZ. At 150℃ and 200℃, the density of the ITZ matrix increases, radial cracks are not significant, and tangential cracks appear in the ITZ matrix.

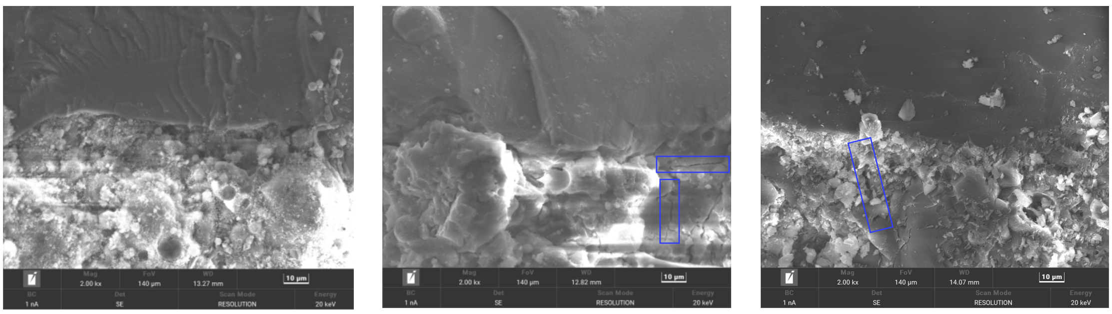

(a) S0-1.5-6, 200℃, 28d (b) S25-1.5-6, 200℃, 28d (c) S50-1.5-6, 200℃, 28d

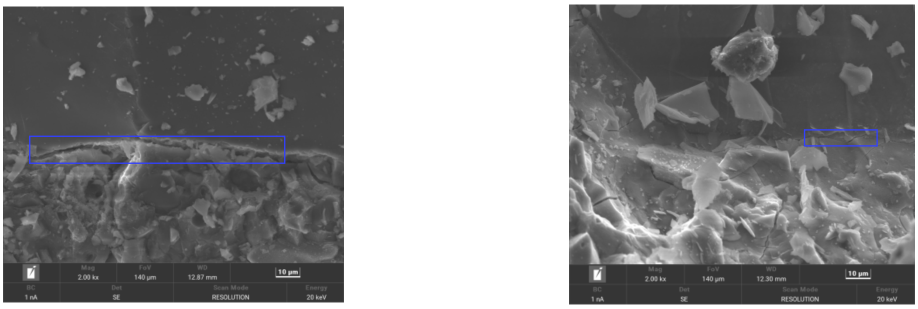

(d) S75-1.5-6, 200°C, 28d (e) S100-1.5-6, 200°C, 28d

Fig.22. ITZ microstructure of AAFS concrete with different fly ash-slag mass ratios

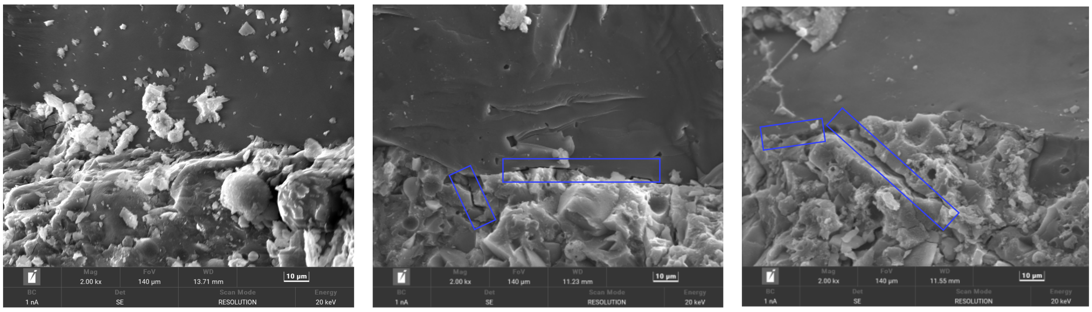

(a) S50-1.5-6, RT (b) S50-1.5-6, 150°C, 3d (c) S50-1.5-6, 150°C, 7d

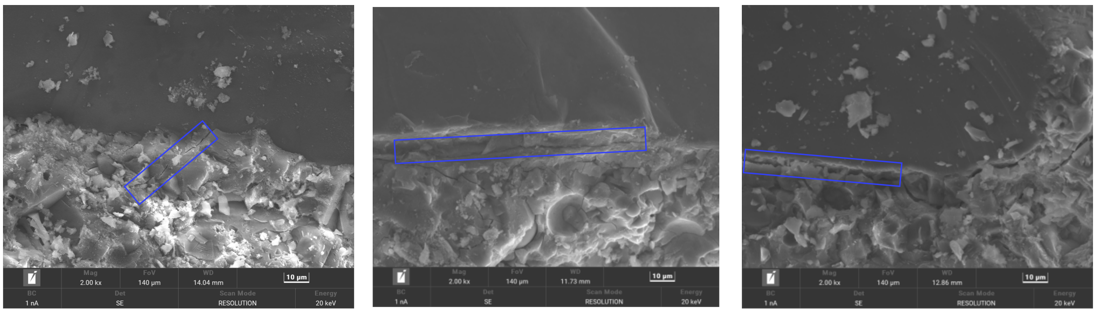

(d) S50-1.5-6, 150°C, 28d (e) S50-1.5-6, 150°C, 60d (f) S50-1.5-6, 150°C, 90d

Fig.23. ITZ microstructure of S50-1.5-6 concrete sample with different duration

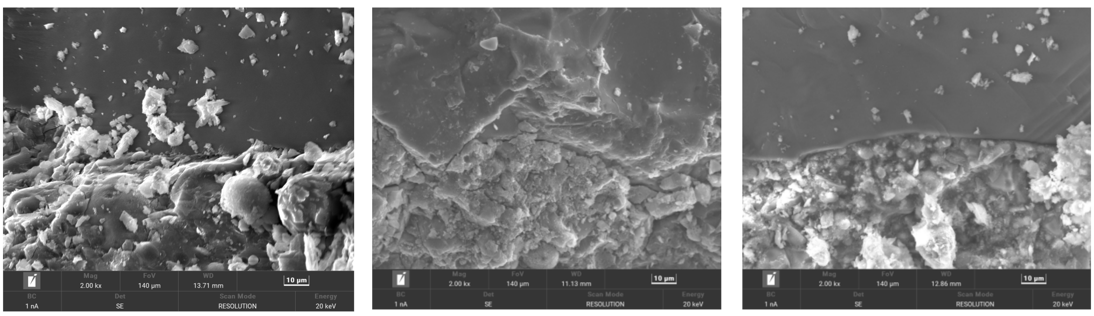

(a) S50-1.5-6, RT (b) S50-1.5-6, 60°C, 28d (c) S50-1.5-6, 100°C, 28d

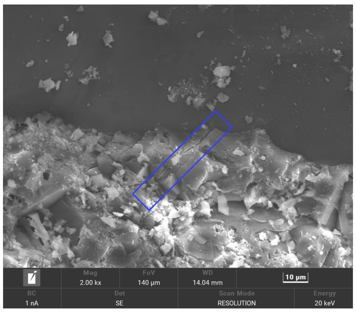

(d) S50-1.5-6, 150℃, 28d

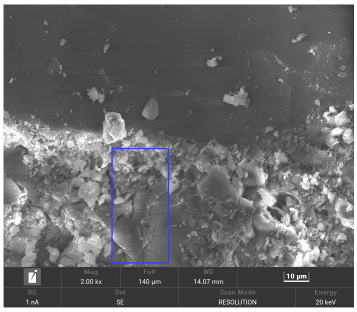

(e) S50-1.5-6, 200℃, 28d

Fig.24. ITZ microstructure of S50-1.5-6 concrete sample with different temperature levels

4 Discussion on the performance evolution mechanism of AAFS concrete under sustained high temperatures

4.1 Variation of 2D fractal dimension of X-CT images

Based on X-CT images, it can be seen that the internal structure and morphology of AAFS concrete are random and disordered, and fractal theory can characterize the complexity of concrete structure. The fractal dimension can express the texture information of X-CT images, and the larger the fractal dimension, the more complex the microstructure [27]. Based on the box dimension method [43], the 2D fractal dimension of X-CT slices is calculated. According to the slice number obtained by X-CT, a slice photo is extracted every 25, and 45 X-CT slice photos are extracted from each group of samples for fractal dimension calculation. Fig.25 shows the 2D fractal dimensions of AAFS concrete by X-CT. With the increase of slag content, the 2D fractal dimension decreases first and then increases, which is consistent with the law of micro-crack change in Fig.9. The less the number and connectivity of micro-cracks, the smaller the fractal dimension. At 150℃, the 2D fractal dimension decreases first and then increases with the increase in duration, and the fractal dimension is the smallest at 28d. At RT, AAFS concrete contains a large number of flocculent, rod-like C-(A)-S-H and N-A-S-H gels, as well as unreacted fly ash particles. The microstructure is more complex, and the fractal dimension is the largest. When the concrete is exposed to high temperatures for 3d and 7d, the internal water loss of the concrete is rapid, the morphology of the gel phases changes from flocculent to block (see Fig.20), and the tensile stress of the capillary pore induces a large number of micro-cracks in the mortar. There are more cracks in the ITZ region (see Fig.23(b) and (c)), and the fractal dimension is large. When the duration reaches 28d, the small blocks are reorganized into large blocks, the number of micro-cracks decreases, and the fractal dimension decreases. As the duration increases to 60d and 90d, the continuous restructuring of hydration products induces an increase in internal micro-cracks (see Fig.10(e) and (f)), the tangential cracks in the ITZ region become wider, the radial cracks increase (see Fig.23(e) and (f)), and the fractal dimension increases. As shown in Fig.25 (c), the fractal dimensions at four temperature levels show a significant decrease and then increase, but the difference is not significant, ranging from 1.805~1.820. The fractal dimensions at the four temperature levels are significantly reduced compared to the RT environment. The 2D fractal dimension can be used to qualitatively evaluate the internal micro-cracks and microstructure morphology of AAFS concrete after continuous high temperatures.

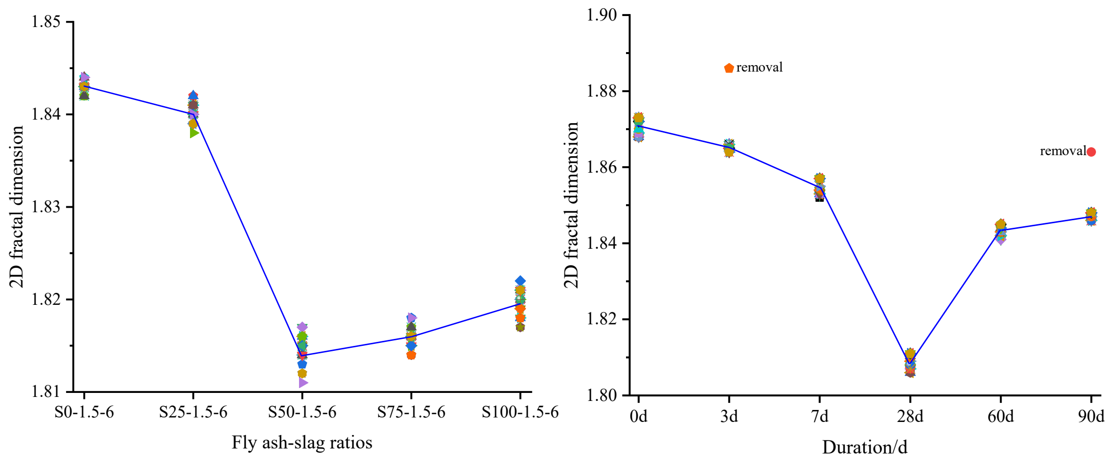

(a) Fly ash-slag ratios (b) Duration, S50-1.5-6, 150°C

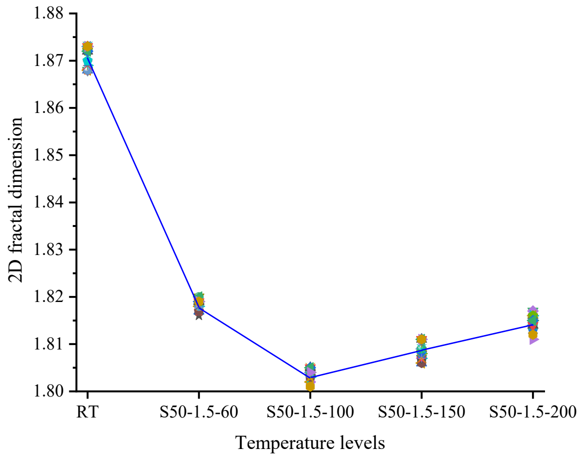

(c) Temperature levels, S50-1.5-6, 28d

Fig.25. 2D fractal dimensions of AAFS concrete by X-CT

4.2 Evolution mechanism of AAFS concrete properties

Sustained high temperatures lead to physical and chemical changes in the internal phases of alkali-activated concrete [44]. The presence of water between the gel phase layers makes the gel phase layers a weak area. After the interlayer water loss, a large tensile stress appears between the gel phases, and the rearrangement degree of the silicon chains in the gel phase is enhanced under the tensile stress. The differential thermal expansion between alkali-activated pastes, aggregates, and water can produce micro-cracks [45-47], especially damage to ITZ. Based on X-CT and SEM tests, it is found that there are two obvious cracks, including tangential cracks in ITZ and radial cracks in the mortar matrix. The ITZ region is not a completely weak area, and there are penetrating micro-cracks in the mortar matrix between the aggregates. Based on the X-CT images, the radial cracks of the matrix are mainly observed, and the SEM images can observe the obvious crack distribution in the ITZ region. With the increase in slag content, the AAFS mortar matrix strength increases, the observed ITZ tangential cracks increase, and the length and width of radial cracks increase. With the increase in duration, the number of cracks decreases first and then increases, and dense microstructure is observed at 28d. The duration for 3d and 7d are mainly radial cracks, which are related to water loss. When the duration is 60d or 90d, wide and long tangential crack appears, mainly due to the reorganization and shrinkage of the matrix, resulting in a large tensile stress in the ITZ region. 60°C is the lower temperature (generally 50°C~120°C) for gel phases bound water decomposition [48]. The stable gel phases do not lose water for a short or even a long time. Due to the slow water loss, the water-filled pores form planum semilunar to generate capillary pressure, and the number of micro-cracks is greater. At 100°C, the unstable gel phases bound water completely loses water at 3d (see Fig.8(c)), and there is still a stable gel phase containing bound water in the system, increasing the volume of transition pore and decreasing the number of micro-cracks. At 150 °C, the gel phases bound water loss and restructuring process accelerates, and the matrix micro-cracks increase. However, due to the restructuring of the matrix into a block, the cumulative porosity and pore volume of each part are the lowest. The mass loss rate at 200 °C is larger, which may be related to the decomposition of the gel phases. The number of micro-cracks increases, and only the volume of transition pore increases significantly. With the appearance of gel pore, the effect of 200°C increases the proportion of pore volume $<0.1\mu m$ and refines the pore size. At 100°C, 150°C, and 200°C, the mass loss rate can be stable in 3d-7d (see Fig.8), and cause a large number of micro-cracks. When the duration is 28d, the micro-cracks of the sample are the least and the cumulative pore volume is the smallest, which indicates that there is no cumulative effect of internal micro-cracks and pores caused by the early high-temperature effect. Internal damage of duration for 28d, 60d, and 90d has a cumulative effect.

Except for S0-1.5-6, S50-0.5-6, and S50-1.0-6 samples, the compressive strength of other samples decreases significantly after the duration for 3d, which is different from the changes of AAFS paste samples tested by the previous research group [17]. The decrease in compressive strength is related to the increase of micro-cracks and pore volume caused by water loss, especially the increase significantly of large pore volume. When the duration is 7d and 28d, the compressive strength increases. It is mainly related to the restructuring of hydration products, and the internal structure of the matrix is agglomerated into blocks. Based on X-CT images, the number of micro-cracks decreases at 28d, and the SEM test shows that the number of tangential and radial cracks in ITZ decreases.Based on the MIP test, the large pore volume and cumulative porosity decrease obviously. When the duration is 60d and 90d, the compressive strength decreases, which has nothing to do with the mass loss at this time, mainly related to the change of internal pore structure and micro-cracks. During the restructuring of hydration products, the volume of capillary and large pores increases significantly, the number of micro-cracks increases, and there are obvious tangential wide cracks in the ITZ region.

Based on X-CT and MIP, we tested the pore volumes at two distinct scales in AAFS concrete. The X-CT results demonstrated that incorporating slag effectively reduced the pore volumes of pores smaller than 0.3 mm^3 and larger than 1 mm^3, resulting in a continuous decline in total porosity. Notably, changes in the pore volume of pores smaller than 0.3 mm^3 emerged as a significant factor influencing the mesoscale pore volume, with the lowest porosity observed at 150°C and under sustained high temperatures for 28d. Meanwhile, the MIP test results indicated that variations in the volumes of transition pores and capillary pores were crucial in affecting the microscale pore volume. Specifically, the increase in slag content effectively decreased the volume of capillary pores, while the reduction in the volume of transition pores at 150°C and under sustained high temperatures for 28d was the primary reason for the decrease in cumulative pore volume. Comparing the data from Figs. 15, 16(c), 17(c), and 18(c), it was evident that the patterns of total pore volume variation at the mesoscale were fully aligned with those at the microscale, indicating that AAFS concrete exhibits heterogeneity and that its internal pore structure undergoes intense and prolonged changes under sustained high temperatures, yet these changes at both scales are synergistic.

5 Conclusions

This paper studied the meso-scale and micro-scale pore structure and micro-cracks evolution of AAFS concrete under sustained high temperatures to explain the evolution mechanism of macro-scale mechanical properties. The specific conclusions are as follows:

(1) The compressive strength of most AAFS concrete decreases significantly after 3d of sustained high temperature, then increases first and then decreases with the increase of duration. Except for S0-1.5-6, S50-0.5-6, and S50-1.0-6 samples, the compressive strength of other AAFS concrete after the duration for 90d is lower than that of the RT environment.

(2) The dehydration of N-A-S-H gel is rapid at 60°C~200°C. The mass loss of C-S-H and C-A-S-H gel phases at 60°C is continuous, and the duration is about 60d. Based on the mass loss rate results under different fly ash-slag mass ratios, the bound water of the calcium-containing gel phase is more stable than the sodium-containing gel phase at 60°C and 100°C.

(3) With the increase in slag content, the number and length of radial cracks increase significantly, tangential cracks appear, and the crack width is about 0.1mm~0.6mm. A large number of slender radial cracks appeared in the AAFS concrete after sustained high temperatures for 3d. The number and length of micro-cracks are reduced after the duration is 28d, and the internal structure is dense. After 90d, the micro-cracks spread all over the sample surface, tangential cracks appear at the ITZ, and the number and width of cracks increase significantly.

(4) With the increase of slag content and duration, the 2D fractal dimension decreases first and

then increases, and the less the number and connectivity of micro-cracks, the smaller the fractal dimension. The four temperature levels have no significant effect on the 2D fractal dimension. The 2D fractal dimension can qualitatively evaluate the internal micro-cracks and microstructure morphology of AAFS concrete after sustained high temperatures.

(5) Under sustained high temperatures, the internal pore structure changes of AAFS concrete become severe and lasting, and there is no cumulative effect of internal micro-cracks and pores caused by early high temperatures. The variation law of pore volume obtained at the meso-scale is completely consistent with the micro-scale.

Credit authorship contribution statement

Hongqiang Ma: Funding acquisition, Writing-review and editing

Congcong Fu: Data processing, Original manuscript writing

Jialong Wu: Data processing

Xinhua Yuan: Data processing

Chao Wu: Writing-review and editing

Jingjing Feng: Funding acquisition

Declaration of competing interest

The authors declare that they have no conflict of interest.

Acknowledgments

This research was funded by the National Natural Science Foundation of China (52178227 and

52478263), Natural Science Foundation of Hebei Province (E2022201011).

References

[1] S.A. Miller, A. Horvath, P. Monteiro, Impacts of booming concrete production on water resources worldwide, Nat. Sustain. 1(1) (2018) 69-76.

[2] S.A. Miller, V.M. John, S.A. Pacca, A. Horvath, Carbon dioxide reduction potential in the global cement industry by 2050. Cem. Concr. Res. 114 (2018) 115-124.

[3] Q.F. Liu, Y.X. Cai, H. Peng, Z.Z. Meng, S. Mundra, A. Castel, A numerical study on chloride transport in alkali-activated fly ash/slag concretes, Cem Concr Res. 166 (2023) 107094.

[4] Z. Liu, J. Du, W.N. Meng, Achieving low-carbon cementitious materials with high mechanical properties using $CaCO_3$ suspension produced by CO_2 sequestration, J. Clean. Prod. 373 (2022) 133546.

[5] R.L. Cao, S.Q. Zhang, Z.J. Jia, C. Chen, Z.H. Zhang, N. Banthia, Y.Y. Gao, Y.M Zhang, Influence of ferronickel slag on the reaction kinetics and microstructure of alkali-activated slag, Cem. Concr. Compos. 142 (2023) 105173.

[6] J.L. Provis, Alkali-activated materials, Cem. Concr. Res. 114 (2018) 40-48.

[7] C.J. Shi, A.F. Jiménez, A. Palomo, New cements for the 21st century: the pursuit of an alternative to Portland cement, Cem. Concr. Res. 41 (2011) 750-763.

[8] C. Liu, X.H. Liang, Y. Chen, Z.M. Li, G. Ye, Degradation of alkali-activated slag subjected to water immersion, Cem. Concr. Compos. 142 (2023) 105157.

[9] W.L. Tu, Y. Zhu, G.H. Fang, X.G. Wang, M.Z. Zhang, Internal curing of alkali-activated fly ash-slag pastes using superabsorbent polymer, Cem. Concr. Compos. 116 (2019) 179-190.

[10] P. Chen, Q. Chen, Y. Fang, C. Wang, X. Wang, J. Li, Y. Wang, Preparation of shrinkage-free alkali-activated slag material using MgO as both the activator and the expansive agent, Mater. de Constr. 73(349)(2023) e306.

[11] Y. Li, J.L. Shen, H. Lin, Y.Q. Li, Optimization design for alkali-activated slag-fly ash geopolymer concrete based on artificial intelligence considering compressive strength, cost, and carbon emission, J. Build. Eng. 75 (2023) 106929.

[12] J. Zhang, C.J. Shi, Z.H. Zhang, X. Hu, Reaction mechanism of sulfate attack on alkali-activated slag/fly ash cements, Constr. Build. Mater. 318 (2022) 126052.

[13] M.N.N. Khan, P.K. Sarker, Effect of waste glass fine aggregates on the strength, durability and high temperature resistance of alkali-activated fly ash and GGBFS blended mortar, Constr. Build. Mater, 263 (2020) 120177.

[14] V. Ponomar, E. Adesanya, K. Ohenoja, M. Illikainen, High-temperature performance of slag-based Fe-rich alkali-activated materials, Cem. Concr. Res. 161 (2022) 106960.

[15] O. Burciaga-Díaz, J.I. Escalante-García, Comparative performance of alkali activated slag/metakaolin cement pastes exposed to high temperatures, Cem. Concr. Compos. 84 (2017) 157-166.

[16] H.A. Abdel-Gawwad, A.M. Abbass, H. Al-kroom, P. Sikora, A.M. El-Khayatt, M.A. Elrahman, D. Stephan, Understanding the role of andesite igneous rock in enhancing the performance of alkali-activated ultrafine slag exposed to normal and elevated temperatures, Constr. Build. Mater. 409 (2023) 133847.

[17] H.Q. Ma, C. Wu, Mechanical and microstructural properties of alkali-activated fly ash-slag material under sustained moderate temperature effect, Cem. Concr. Compos. 134(2022) 104744.

[18] H. EI-Didamony, A.A. Amer, H.A. Ela-ziz, Properties and durability of alkali-activated slag pastes immersed in sea water, Ceram. Int. 38(5) (2012) 3773-3780.

[19] L. Luo, W. Yao, G.W. Liang, Y. Luo, Workability autogenous shrinkage and microstructure of alkali-activated slag/fly ash slurries: effect of precursor composition and sodium silicate modulus, J. Build. Eng. 73 (2023) 106712.

[20] M. Sarıdemir, M. Bulut, U. Akca, Effects of different curing conditions on the long-term properties of alkali activated GBP+GBFS mortars exposed to high temperatures, Constr. Build. Mater. 321 (2022) 125732.

[21] Q. Zhang, G. Ye, Dehydration kinetics of portland cement paste at high temperature, J. Therm. Anal. Calorim. 110 (2012) 153-158.

[22] P. Duxson, G.C. Lukey, J.S.J. van Deventer, The thermal evolution of metakaolin geopolymers: Part 2-phase stability and structural development, J. Non-Cryst. Solids. 353(22-23) (2007) 2186-2200.

[23] Q. Zeng, S. Chen, P.C. Yang, Y. Peng, J.Y. Wang, C.S. Zhou, Z.D. Wang, D.M. Yan, Reassessment of mercury intrusion porosimetry for characterizing the pore structure of cement-based porous materials by monitoring the mercury entrapments with X-ray computes tomography, Cem. Concr. Compos. 113 (2020) 103726.

[24] H.Y. Ma, Mercury intrusion porosimetry in concrete technology: tips in measurement, pore structure parameter acquisition and application, Journal. of. Porous. Materials. 21 (2014) 207-215.

[25] Y.R. Zhang, S.X. Xu, Y.H. Gao, J. Guo, Y.H. Cao, J.Z. Zhang, Correlation of chloride diffusion coefficient and microstructure parameters in concrete: a comparative analysis using NMR, MIP, and X-CT, Front. Struct. Civil. Eng. 14(6) (2020) 1509-1519.

[26] X.X. Dong, X.H. Bao, H.Z. Cui, C.J. Xu, X.S. Chen, Macro-porosity and skeleton of a cement-gravel-treated granite residual soil for subgrade from CT scanning, Constr. Build. Mater. 371 (2023) 130703.

[27] S.B. Xue, P. Zhang, J.W. Bao, L.F. He, Y. Hu, S.D. Yang, Comparison of mercury intrusion porosimetry and multi-scale X-ray CT on characterizing the microstructure of heat-treated cement mortar, Mater. Charact. 160 (2020) 110085.

[28] T. Meng, H.D. Wei, D.W. Dai, J.P. Liao, S. Ahmed, Effect of brick aggregate on failure process of mixed recycled aggregate concrete via X-CT, Constr. Build. Mater. 327 (2022) 126934.

[29] J.Z. Xiao, N. Han, L.H. Zhang, S. Zou, Mechanical and microstructural evolution of 3D printed concrete with polyethylene fiber and recycled sand at elevated temperatures, Constr. Build. Mater. 293 (2021) 123524.

[30] H.Q. Ma, C.C. Fu, K. Huang, E.Y. Dai, S.C. Zhang, Y.L. Fang, J.J. Feng, Study on the characteristics of alkali-activated fly ash-slag improved by cenosphere: hydration and drying shrinkage, Constr. Build. Mater. 372 (2023) 130822.

[31] K.Y. Kim, T.S. Yun, K.P. Park, Evaluation of pore structures and cracking in cement paste exposed to elevated temperatures by X-ray computed tomography, Cem. Concr. Res. 50 (2013) 34-40.

[32] J.S. Kim, S.Y. Chung, T.S. Han, D. Stephan, M.A. Elrahman, Correlation between microstructural characteristics from micro-CT of foamed concrete and mechanical behaviors evaluated by experiments and simulations, Cem. Concr. Compos. 112 (2020) 103657.

[33] S.Q. Yang, D.P. Zheng, C.S. Poon, H.Z. Cui, In-situ alkali-silica reaction evolution of lightweight aggregate concretes prepared with alkali-activated cement and ordinary portland cement assessed by X-ray micro computed-tomography, Cem. Concr. Compos. 140 (2023) 105108.

[34] H.F. Wang, Z.P. Chen, J. Ren, S.C. Chen, F. Xing, Object status identification of X-ray CT images of microcapsule-based self-healing mortar, Cem. Concr. Compos. 125 (2022) 104294.
[35] H.T. Kim, T. Razakamandimby,V. Szilágyi, Z. Kis, L. Szentmiklósi, M. Glinicki, K. Park, Reconstruction of concrete microstructure using complementarity of X-ray and neutron tomograph, Cem. Concr. Res. 148 (2021) 106540.
[36] S. Puligilla, P. Mondal, Role of slag in microstructural development and hardening of fly ash-slag geopolymer, Cem. Concr. Res. 43 (2013) 70-80.
[37] N. Bossa, P. Chaurand, J. Vicente, D. Borschneck, C. Levard, O. Aguerre-Chariol, J. Rose, Micro- and nano-X-ray computed-tomography: A step forward in the characterization of the pore network of a leached cement paste, Cem. Concr. Res. 67 (2015) 138-147.
[38] W.H. Liu, C. Liu, G.L. Bai, C. Zhu, Study on the effect of chloride ion ingress on the pore structure of the attached mortar of recycled concrete coarse aggregate, Constr. Build. Mater. 263 (2020) 120123.
[39] S.C. Kou, C.S. Poon, M. Etxeberria, Influence of recycled aggregates on long term mechanical properties and pore size distribution of concrete, Cem. Concr. Compos. 33(2) (2011) 286-291.
[40] C. Liu, H.W. Liu, C. Zhu, G.L. Bai, On the mechanism of internal temperature and humidity response of recycled aggregate concrete based on the recycled aggregate porous interface, Cem. Concr. Compos. 103 (2019) 22-35.
[41] J.C. Fan, B. Zhang, Repair of ordinary Portland cement concrete using alkali activated slag/fly ash: Freeze-thaw resistance and pore size evolution of adhesive interface, Constr. Build. Mater. 300 (2021) 124334.
[42] Z.Y. Luo, W.G. Li, K.J. Wang, S.P. Shah, D.C. Sheng, Nano/micromechanical characterisation and image analysis on the properties and heterogeneity of ITZs in geopolymer concrete, Cem. Concr. Res. 152 (2022) 106677.

[43] H.Q. Ma, J.W. Sun, C. Wu, C. Yi, Y. Li, Study on the pore and microstructure fractal characteristics of alkali-activated coal gangue-slag mortars, Mater. 13(11) (2020) 2442.

[44] G. Ye, X. Liu, G. De Schutter, L. Taerwe, P. Vandevelde, Phase distribution and microstructural changes of self-compacting cement paste at elevated temperature, Cem. Concr. Res. 37(6) (2007) 978-987.

[45] R. Loser, B. Munch, P. Lura, A volumetric technique for measuring the coefficient of thermal expansion of hardening cement paste and mortar, Cem. Concr. Res. 40(7) (2010) 1138-1147.

[46] Z. Xing, A.L. Beaucour, R. Hebert, A. Noumowe, B. Ledesert, Influence of the nature of aggregates on the behaviour of concrete subjected to elevated temperature, Cem. Concr. Res. 41(4) (2011) 392-402.

[47] H. Cagnon, T. Vidal, A. Sellier, X. Bourbon, G. Camps, Transient thermal deformation of high performance concrete in the range 20℃~40℃, Cem. Concr. Res. 116 (2019) 19-26.

[48] K.D.T. Thi, M.C. Liao, D.H. Vo, The characteristics of alkali-activated slag-fly ash incorporating the high volume wood bottom ash: mechanical properties and microstructures, Constr. Build. Mate.r 394 (2023) 132240.